

Large Eddy Simulations of the Flow in the Near-Field Region of a Turbulent Buoyant Helium Plume

G. Maragkos · P. Rauwoens · Y. Wang · B. Merci

Received: 16 December 2011 / Accepted: 16 November 2012
© Springer Science+Business Media Dordrecht 2012

Abstract Large eddy simulations are conducted in the near-field region of a large turbulent buoyant helium plume. The CFD package FireFOAM is applied to that purpose. The transient and mean flow dynamics are discussed as a function of grid resolution, with and without the use of the standard Smagorinsky subgrid scale (SGS) model. Small scale structures, formed at the edge of the plume inlet due to baroclinic and gravitational mechanisms and subject to flow instabilities, interact with large scale features of the flow, resulting in a puffing cycle. In general, the LES calculations reproduce the main features of the turbulent plume, with better agreement when the Smagorinsky type SGS model is applied. In particular, the puffing cycle is recovered in the simulations with correct frequency. The mean and rms values of the velocity components are well predicted with use of the SGS model, even on relatively coarse meshes. Agreement for the species mass fraction (mean and rms values) is less satisfactory, but in line with results found in the literature.

Keywords Helium plume · Smagorinsky · LES · FireFOAM

This research has been funded by Ghent University (Belgium) through BOF project 01J01909.

G. Maragkos (✉) · B. Merci
Department of Flow, Heat and Combustion Mechanics, Ghent University,
St. Pietersnieuwstraat 41, 9000 Ghent, Belgium
e-mail: Georgios.Maragkos@UGent.be

P. Rauwoens
Department of Civil Engineering, Ghent University,
Technology Park 904, 9052 Ghent, Belgium
e-mail: Pieter.Rauwoens@UGent.be

Y. Wang
FM Global, Research Division, 1151 Boston - Providence Turnpike,
P.O. Box 9102, Norwood, MA 02062, USA
e-mail: yi.wang@fmglobal.com

1 Introduction

The study of turbulent buoyant helium plumes is interesting for several reasons. First of all, the test case is challenging for CFD codes. Indeed, in the plume, there is a rapid transition from laminar to fully turbulent, usually within a few inlet diameters, created by strong buoyancy forces. The generation of vorticity within the interior of the flow is due to baroclinic and gravitational mechanisms, related to density-pressure gradients and gravity-density gradients, respectively. Two modes of turbulence can be identified [1]. The coherent structures created by puffing vortices and the finger-like structures caused by the Rayleigh-Taylor instability, which enhances mixing. Second, there is an interesting similarity of the flow field (such puffing frequency) to the flow field observed above pool fires.

An important mechanism in this kind of flows is the coupling between the momentum and species equations through density, since the mixture composition determines density through the mixture molecular weight. For buoyant, low Mach-number flows, the source term in the momentum equations is the product of density and gravity, hence, the forcing function for a buoyant flow. This buoyant forcing results in mixing that in turn changes density and thus the two sets of equations are coupled. Turbulence resulting directly from this coupling is referred to as ‘buoyancy generated turbulence’ [2]. It is postulated in [3] that a combination of vorticity generation and vorticity transport mechanisms are responsible for the turbulence created. In Reynolds-Averaged Navier-Stokes (RANS) simulations the turbulence model needs to be adjusted to take this effect into account [4]. In LES, in principle this should be captured automatically with less modeling effort.

Much experimental work has been done on turbulent plumes. Small-scale experiments of buoyant helium plumes were performed by Cetegen et al. [5, 6] in order to identify the mechanism responsible for the periodic oscillations occurring near the plume source. Papanikolaou and List [7] examined a momentum driven buoyant jet, where the buoyancy effects become dominant only far downstream of the source and investigated the turbulence properties and the transition from momentum-driven jets to buoyancy-driven plumes. Shabbir and George [8] did experiments on a turbulent buoyant thermal plume and reported on the effect of buoyancy on turbulent buoyant plumes. In addition several numerical studies of turbulent plumes using DNS and LES have already appeared in the literature. Zhou et al. [9] performed LES of the near and far-field of a spatially-developing round turbulent buoyant plume showing that plumes, like cold jets, can also have several stages of vortex development such as roll-up and breakdown. Soteriou et al. [10] studied the unsteady dynamics of planar plumes using a high-resolution Lagrangian method, emphasizing on the pulsating instability characterizing the source near field. Chung and Devaud [11] studied the near field of a helium plume using buoyancy corrected $k - \epsilon$ models in Reynolds Averaged Navier-Stokes (RANS) calculations and with traditional eddy-viscosity LES methods. Pham et al. [12] performed DNS and LES simulations with the dynamic Smagorinsky eddy-viscosity model of a pure thermal plume and reported on the puffing phenomenon that occurs in the near-field region of the plume source. DesJardin et al. [13] explored the instability modes and flow dynamics of a large

turbulent helium plume, as a function of grid resolution with and without the use of subgrid scale (SGS) models, and reported on the energy transfer from small to large scales, i.e. inverse energy cascade.

In the study at hand, LES results obtained with a slightly modified version of the FireFOAM (<http://code.google.com/p/firefoam-dev>) code are compared to the well-documented experiment performed by O'Hern et al. [14]. FireFOAM is based on the OpenFOAM (<http://www.openfoam.com>) platform, a set of object-oriented open source CFD toolboxes written in C++. It utilizes the finite volume method on unstructured polyhedral meshes and is highly scalable on massively parallel computers [15]. FireFOAM has been developed at FM Global (<http://www.fmglobal.com/modelling>) and is continuously being validated for fire related flow simulations [16, 17]. By applying the code to a non-reacting plume, the effect of buoyancy generated turbulence can be tested, independently of the complexity introduced by turbulent combustion. First we present FireFOAM, introducing the modifications made in the code and analysing the subgrid scale models used for turbulence. Then a detailed description of the experimental set-up is given, followed by the numerical set-up chosen to model the problem. LES results are presented for the mean and rms velocity and concentration profiles in comparison to experimental data, with and without subgrid (SGS) model. The reason why results are presented without SGS model is to access the validity of the conclusions stated in the work by DesJardin et al. [13], namely that the use of the standard Smagorinsky SGS model would give worse predictions for this kind of flows, as compared to results obtained without SGS model. The analysis also includes a sensitivity study on the Smagorinsky constant, C_s , and the turbulent Schmidt number, Sc_t .

The specific motivation for this study, focusing on large eddy simulations (LES) in the near-field region of a large axisymmetric turbulent buoyant helium plume, is therefore two-fold. Firstly, to get a better insight of the buoyancy generated turbulence and the generation of the Rayleigh-Taylor instability that determines the puffing cycle of the plume. This behavior is similar to the puffing frequency observed in pool fires and a better understanding of this mechanism will help to understand more about the flow dynamics in this kind of flows. Secondly, the validation of the FireFOAM code in buoyancy driven flows, an application that has similar turbulent mixing characteristics with fire scenarios. The validation of the code will be of great interest to the fire community and will give the opportunity to more researchers to use it for fire related applications.

2 FireFOAM

A modified version of FireFOAM is used in this study. The default energy equation and equation of state have been removed, and mixture density is directly calculated from the species concentration. It solves for the low-Mach number form of the Navier-Stokes equations, using Favre-filtered quantities, along with a transport equation for helium mass fraction for a non-reacting, isothermal system. Equal

diffusivities are assumed for all species. Filtering the instantaneous balance equations leads to the following transport equations for mass, momentum and species:

$$\frac{\partial \bar{\rho}}{\partial t} + \frac{\partial \bar{\rho} \tilde{u}_i}{\partial x_i} = 0 \quad (1)$$

$$\frac{\partial \bar{\rho} \tilde{u}_j}{\partial t} + \frac{\partial \bar{\rho} \tilde{u}_i \tilde{u}_j}{\partial x_i} = -\frac{\partial \bar{p}}{\partial x_j} + \frac{\partial \bar{\tau}_{ij}}{\partial x_i} + \frac{\partial \bar{\tau}_{ij}^{sgs}}{\partial x_i} + \bar{\rho} g_i \quad (2)$$

$$\frac{\partial \bar{\rho} \tilde{Y}}{\partial t} + \frac{\partial \bar{\rho} \tilde{u}_i \tilde{Y}}{\partial x_i} = -\frac{\partial \bar{q}_i}{\partial x_i} - \frac{\partial \bar{q}_i^{sgs}}{\partial x_i} \quad (3)$$

where $\bar{\rho}$ is the filtered mixture density, \tilde{u} is the velocity vector, \bar{p} is the pressure and \tilde{Y} is the helium mass fraction. The filtered viscous stress tensor $\bar{\tau}_{ij}$ and species diffusion \bar{q}_i are modeled by Newton's and Fick's laws, in terms of resolved quantities:

$$\bar{\tau}_{ij} = \mu_l \left(\frac{\partial \tilde{u}_i}{\partial x_j} + \frac{\partial \tilde{u}_j}{\partial x_i} \right) - \frac{2}{3} \mu_l \frac{\partial \tilde{u}_k}{\partial x_k} \delta_{ij} \quad (4)$$

$$\bar{q}_i = -\frac{\mu_l}{Sc} \frac{\partial \tilde{Y}}{\partial x_i} \quad (5)$$

where the laminar viscosity of fuel is calculated by the experimental conditions and inlet Reynolds number as $\mu_l = 1.8774 \times 10^{-5}$ kg/ms, the molecular Schmidt number is given the value $Sc = 0.2$ [13] and δ_{ij} is the Kronecker symbol: $\delta_{ij} = 1$ if $i = j$, 0 otherwise.

Filtered density, $\bar{\rho}$, is a function of helium and air composition. Thus, the mixing induced by the momentum equations yields:

$$\bar{\rho} = \rho_f \bar{\phi}_f + \rho_{\text{air}} (1 - \bar{\phi}_f) \quad (6)$$

where $\bar{\phi}_f$ is the filtered volume fraction of helium and ρ_f , ρ_{air} are the densities of helium and air respectively, calculated by the ideal gas law. The volume fraction of fuel is related to its mass fraction, solved by the transport equation, as:

$$Y = \frac{\rho_f \bar{\phi}_f}{\rho_f \bar{\phi}_f + \rho_{\text{air}} (1 - \bar{\phi}_f)} \implies \bar{\phi}_f = \frac{\rho_{\text{air}} Y}{\rho_f + \rho_{\text{air}} Y - \rho_f Y} \quad (7)$$

Figure 1 illustrates how the mixture density, ρ , varies with the helium volume fraction ϕ_f . Densities of air and helium are $\rho_{\text{air}} = 0.987$ kg/m³ and $\rho_f = 0.186$ kg/m³ respectively, in agreement with the conditions of the experiment presented in the next section.

The widely used standard Smagorinsky model [18] is used for closure of the subgrid scale stress terms in the momentum equations. It is an eddy viscosity type model where the unresolved SGS stress terms, $\bar{\tau}_{ij}^{sgs} = \bar{\rho}(\tilde{u}_i \tilde{u}_j - \tilde{u}_i \tilde{u}_j)$, are expressed according to the Boussinesq assumption as:

$$\bar{\tau}_{ij}^{sgs} + \frac{1}{3} \bar{\rho} \delta_{ij} \tau_{kk} = \mu_{sgs} \left(\frac{\partial \tilde{u}_i}{\partial x_j} + \frac{\partial \tilde{u}_j}{\partial x_i} \right) = 2 \mu_{sgs} \bar{S}_{ij} \quad (8)$$

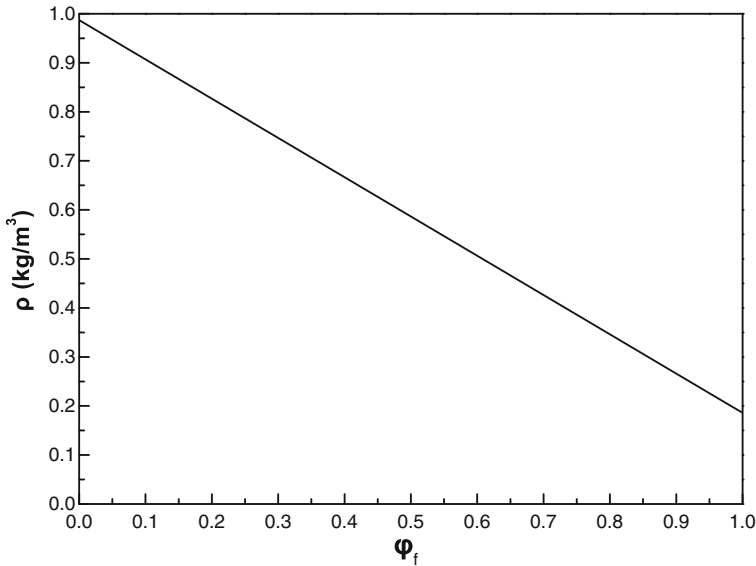


Fig. 1 Density as a function of fuel volume fraction ϕ_f

where \bar{S}_{ij} is the strain rate tensor component and the subgrid scale viscosity, μ_{sgs} , is modelled as:

$$\mu_{sgs} = \bar{\rho}(C_s \Delta)^2 |\bar{S}| \quad (9)$$

where C_s is a model constant, $|\bar{S}| = \frac{1}{2}(\nabla \tilde{u} + \nabla \tilde{u}^T)$ is the rate of strain tensor and Δ is the filter size taken to be, $\Delta = (\Delta x \Delta y \Delta z)^{\frac{1}{3}}$, with Δx , Δy and Δz the effective grid mesh spacings. In the case of homogeneous isotropic turbulence, the model constant is estimated as $C_s \approx 0.2$ [19]. However, the Smagorinsky model is known to be too dissipative and C_s depends on the flow configuration so values of $C_s \approx 0.1 - 0.2$ are often used [20]. A constant of $C_s = 0.1$ is used in this study. A sensitivity analysis on the model constant is presented in Section 7.

The un-resolved subgrid scale species fluxes, $\bar{q}_i^{sgs} = \bar{\rho}(\tilde{u}_i \tilde{Y} - \tilde{u}_i \tilde{Y})$, in the species transport equation are modelled by the gradient diffusion hypothesis model as:

$$\bar{q}_i^{sgs} = -\frac{\mu_{sgs}}{Sc_t} \frac{\partial \tilde{Y}}{\partial x_i} \quad (10)$$

assuming a constant turbulent Schmidt number of $Sc_t = 0.5$ [11]. A sensitivity study on this value is presented in Section 7.

3 Experimental Case

In this study comparisons are made to results from experiments performed in the Fire Laboratory for Accreditation of Models and Experiments (FLAME) at Sandia

National Laboratories in Albuquerque, New Mexico, as reported by O'Hern et al. [14]. In the experiments two planar imaging techniques were simultaneously applied: particle image velocimetry (PIV) for velocity field measurements and planar laser-induced fluorescence (PLIF) for scalar field measurements (mass fraction).

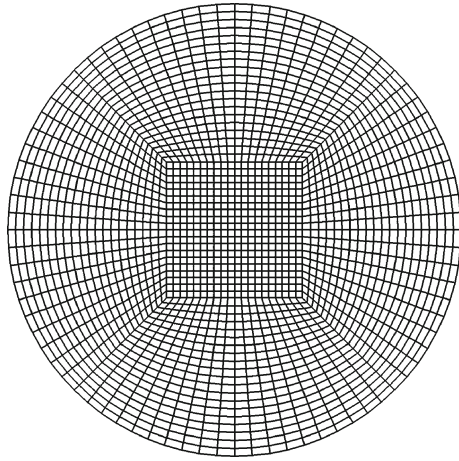
The FLAME chamber consists of a 6.1 m cubical enclosure with a 2.4 m in diameter chimney located on top of the chamber. The experiment was designed to be a canonical buoyant plume so that the results would not be dependent on the specific experimental geometry. The plume source is 1 m in diameter, surrounded by a 0.51 m wide floor, the 'ground plane'. The plume was developed using helium issuing from the diffuser at an average velocity of 0.325 m/s. A detailed analysis of the spatial velocity distribution of the plume inlet (using air instead of helium) showed that the inlet velocity profile was uniform to within $\pm 6\%$ [21]. For PLIF measurements, $1.7 \pm 0.1\%$ vol. acetone was injected into the helium flow as the fluorescent tracer gas. In addition $1.9 \pm 0.2\%$ vol. oxygen was added to quench acetone phosphorescence. The molecular weight of the helium/acetone/oxygen mixture was $5.45 \pm 2.7\%$ g/mol. The average mixture Reynolds number was $Re = DV_o/\nu = 3200 \pm 0.6\%$, where D is the diameter of the plume source, V_o is the inlet velocity and ν the kinematic viscosity of the helium/acetone/oxygen mixture. The average mixture Richardson number was $Ri = (\rho_\infty - \rho_p)gD/(\rho_\infty V_o^2) = 76 \pm 6.5\%$, with ρ_∞ the external (air) density, ρ_p the plume fluid density and g the acceleration due to gravity. The experiment was performed at a low ambient pressure of $P_\infty = 80900$ Pa (due to the high altitude in which the facility was located) and at temperature $T_\infty = 285$ K.

The experimental uncertainty on the measured velocities and turbulent statistics are in the order of 20 % and 30 %, respectively. The values of concentration contain uncertainties in the order of 18 %, plus fixed uncertainties of 5 %, while the uncertainty on the concentration fluctuation in the order of 21 %. The above uncertainties also include run-to-run variability [14].

4 Numerical Set-up

The simulations are performed on a cylindrical mesh, 4 m in diameter and 4 m in the axial direction, with a rectangular grid in the core ($0.3 \text{ m} \times 0.3 \text{ m}$). A 1 m diameter inflow of helium, located in the center of the bottom plane, is surrounded by a 0.5 m wide wall, which simulates a 'ground plane' causing air being entrained by the accelerating plume to flow radially inward over the floor. The inlet patch at the bottom plane consists of a uniform rectangular grid surrounded by a cylindrical mesh, shown in Fig. 2. The grid resolution for the inlet patch in the coarse grid is set to 10×10 cells (rectangular) and 10×40 (cylindrical) resulting in a total of 500 cells. The grid resolution for the inlet patch in the fine grid is set to 20×20 cells (rectangular) and 20×80 (cylindrical), resulting in a total of 2000 cells. Outside the inlet patch 40 (coarse) or 80 (fine) cells were uniformly spaced radially. In the axial direction 75 (coarse) and 150 (fine) cells were used respectively. The total number of cells is then 157500 (coarse) or 1.26 million cells (fine). The grid has been compressed near the bottom of the plume source, ($y = 0 \text{ m}$), resulting in a minimum and maximum grid spacing of 2.54 cm, 10.75 cm (coarse) and 1.23 cm, 5.39 cm (fine), respectively.

Fig. 2 Schematic representation of the mesh used in the fuel inlet in the simulations



The governing equations are advanced in time using a second order implicit ‘backward’ scheme. All quantities are assigned to the cell centers (collocated grid) with velocities linearly interpolated to the cell faces. The convective terms are second order centrally differenced using ‘Gauss linear’. No purely upwind schemes were used since the use of upwinding in LES can introduce undesirable artificial numerical dissipation, as has been noted by many studies, e.g. [22]. This was also noted in the present study where different schemes have been tested for discretizing the convective terms. Any blending of the linear scheme with upwind resulted in high levels of numerical dissipation (not shown here). For scalar transport, the bounded second order TVD scheme ‘limitedLinear01’ is used while the diffusive terms are centrally differenced and corrected for the non orthogonality of the mesh with ‘Gauss linear corrected’. A PISO algorithm is used for the pressure-velocity coupling with a Rhie-Chow interpolation to avoid odd-even decoupling. The pressure equation is solved by a linear GAMG solver. The reader is referred to (<http://www.openfoam.com>) for details on these options.

The bottom plane of the domain at $y = 0$ m employs a zero fixed value BC for the cross-stream velocities and fixes the streamwise velocity of the inlet to $U_{\text{inlet}}^{\text{fuel}} = 0.325$ m/s in the core of the plume and to a small coflow velocity $U_{\text{coflow}}^{\text{air}} = 0.01$ m/s outside the ‘ground plane’ surrounding the plume inlet. At the ‘ground plane’ the coflow velocity is set to zero. A ‘zeroGradient’ BC is assigned for velocity at the sides of the domain and ‘totalPressure’ BC for pressure. For the top outlet plane an ‘inletOutlet’ BC is used for velocity and ‘zeroGradient’ for pressure. The ‘inletOutlet’ BC assigns a ‘zeroGradient’ for outward velocity and fixes the inlet velocity to zero. The inlet BC for the mass fraction of ‘fuel’ is set to uniform ‘fixedValue 1.0’. Details on the implementation of the BC’s can be found in (<http://www.openfoam.com>) (Table 1).

At every point in the domain, the composition of the gas phase corresponds to a mixture of helium and air. Air has molecular weight $W_{\text{air}} = 28.9$ g/mol while the experimental mixture of helium (He, 96.4 % by vol.), acetone (CH_3COCH_3 , 1.7 % by vol.) and oxygen (O_2 , 1.9% by vol.) is treated as a single gas with molecular weight $W_f = 5.45$ g/mol. Ambient (inlet) temperature and pressure are $T = 285$ K and $P =$

Table 1 Boundary conditions as specified in the simulations (OpenFOAM terminology (<http://www.openfoam.com>))

Surface	Velocity	Dynamic pressure	Mass fraction	Temperature
Inlet	fixedValue 0.325	zeroGradient	fixedValue 1.0	fixedValue 285
CoFlow	fixedValue 0.01	zeroGradient	fixedValue 0.0	fixedValue 285
Sides	zeroGradient	totalPressure	inletOutlet	inletOutlet
Outlet	inletOutlet	zeroGradient	inletOutlet	inletOutlet
Plate	fixedValue 0.0	zeroGradient	fixedValue 0.0	fixedValue 285

80900 Pa, respectively, to match the experimental conditions. The resulting Reynolds and Richardson numbers are $Re = 3220$ and $Ri = 75.3$.

The LES calculations are set up to run for 30 s. The first 20 s allow for the initial computational flow transients to move downstream and to reach statistically stationary flow conditions. Results from the final 10 s of the simulation are compiled to produce density-weighted, time-averaged quantities. A constant time step is used in the simulations ($t_{\text{coarse}} = 0.0005$ s and $t_{\text{fine}} = 0.00025$ s), corresponding to an average Courant number of $Co \approx 0.2$. A domain decomposition parallelization strategy was employed by dividing the computational domain into equally sized mesh blocks across 12 processors. The total physical running time for the coarse and fine mesh was 11 h and 195 h, respectively, on a Dell PowerEdge R610 server with 2× Six-core Intel Xeon X5680, 3.33 GHz and 48GB RAM.

5 Results

5.1 Instability modes

Figure 3 presents instantaneous snapshots of the density field over one puffing cycle, in which the generation of the instabilities near the base of the plume is evident (Fig. 3a, b) due to the misalignment of vertical pressure gradient and density gradient pointing radially outwards (baroclinic torque), generating localized torque as shown in Fig. 4. These instabilities grow in size and eventually form large coherent structures (Fig. 3c, d). These processes repeat themselves in every puffing cycle.

Figure 4 shows the generation of the localized torque discussed above, generated by the misalignment of density and pressure gradients at the beginning of the simulation, at the base of the plume, where helium is released into still air. It consists of snapshots of density, covering half of the inlet plume diameter, with superimposed density (white arrows) and pressure gradients (black arrows) showing the rollup of the vortex at the plume edge.

The inflow conditions of the plume in this buoyancy driven flow are laminar [14]. However, strong turbulent structures form at the helium - air interface very close to the plume source, Fig. 3b. The lack of source turbulence and the strong deflection of the low velocity helium plume from the inlet vertical direction at the edges of the plume, indicate that vorticity from the plume source is not responsible for the formation of these turbulent structures at the helium - air interface. Rather, they are formed by buoyancy-driven (gravitational and baroclinic) vorticity generation. This vorticity generation mechanism will trigger the Rayleigh-Taylor and Kelvin-Helmholtz instabilities, near the base of the plume, and eventually form toroidal vortices [13, 14], shown in Figure 3d.

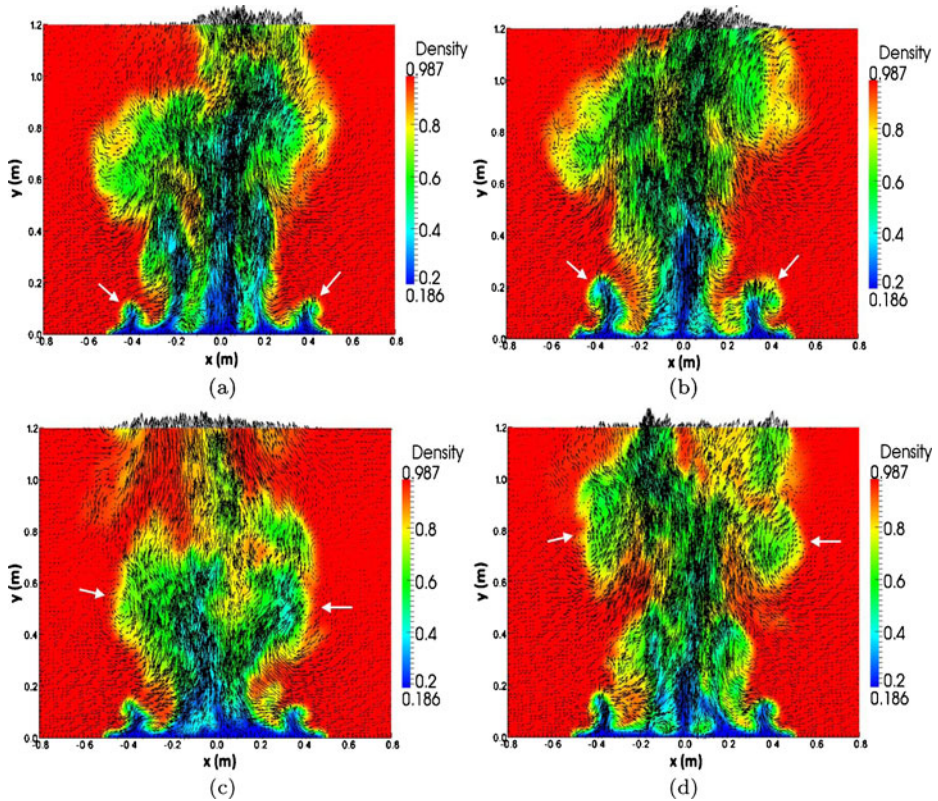


Fig. 3 Instantaneous snapshots of a typical puffing cycle from LES showing isocountours of density (kg/m^3) with superimposed velocity magnitude (m/s) vectors for the fine grid with SGS model at times **a** 10.2 s, **b** 10.26 s, **c** 10.74 s and **d** 11.02 s

5.2 Vortex dynamics

An analysis of the vorticity equation provides a better understanding of how vorticity is generated and transported downstream by convection and diffusion:

$$\frac{D\omega}{Dt} = \underbrace{(\omega \cdot \nabla)V}_{\text{vortex stretching}} - \underbrace{\omega(\nabla \cdot V)}_{\text{dilatation term}} + \underbrace{\frac{1}{\rho^2}(\nabla \rho \times \nabla p)}_{\text{baroclinic torque}} + \underbrace{\frac{\rho_\infty}{\rho^2}(\nabla \rho \times g)}_{\text{gravitational torque}} + \underbrace{\nabla \times \left(\frac{1}{\rho} \nabla \cdot \tau \right)}_{\text{viscous diffusion}} \quad (11)$$

Five different physical mechanisms affect the vorticity transport. The terms on the right hand side of the vorticity equation are identified [23] as vortex stretching term, dilatation term, baroclinic torque, gravitational torque and viscous diffusion. In incompressible flows, only the first term prevails. Vortex stretching is a very important mechanism in the turbulent dynamics as it represents the enhancement of vorticity by stretching. It is the mechanism by which turbulent energy is transferred to smaller scales. The dilatation term represents the effects of expansion of the vorticity

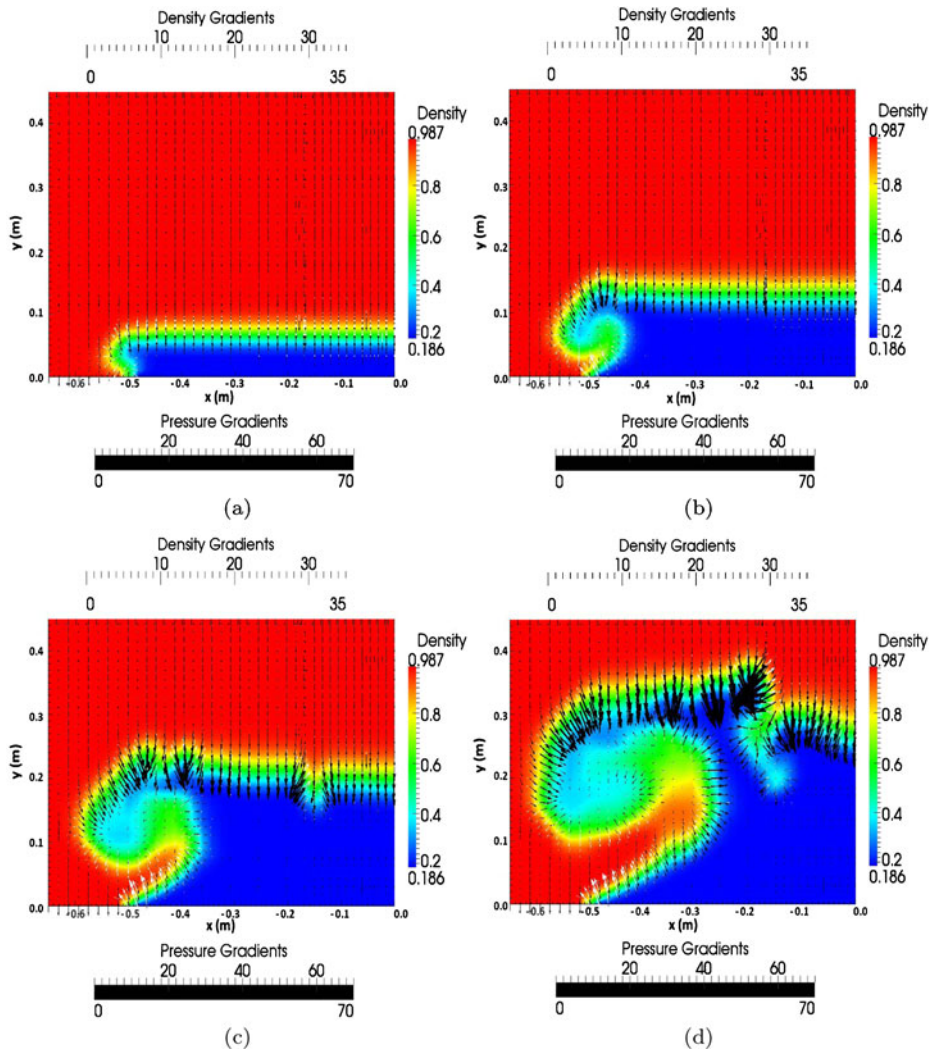


Fig. 4 Misalignment of density gradients (kg/m^4) (white arrows) and pressure gradients ($\text{kg/m}^2\text{s}^2$) (black arrows) near the base of the plume at times **a** 0.2 sec, **b** 0.4 sec, **c** 0.6 sec and **d** 0.8 sec

field and results in a decrease in the magnitude of vorticity (minus sign in Eq. 11). Gravitational torque generates vorticity due to non-aligned gravity and density gradients, while baroclinic torque is the mechanism by which vorticity is generated from non-aligned pressure and density gradients. In buoyancy-driven flows, both the baroclinic and gravitational torque terms, along with vortex stretching, are the main mechanisms promoting flow vorticity [24, 25]. A DNS study [23] identified the gravitational term as key mechanism promoting cross-streamwise vorticity. DesJardin et al. [13] showed that, during a typical puffing cycle, the maximum gravitational torque is located at the base of the plume. Similar behavior is also observed in the current study, as seen in Fig. 5, in which the maximum gravitational

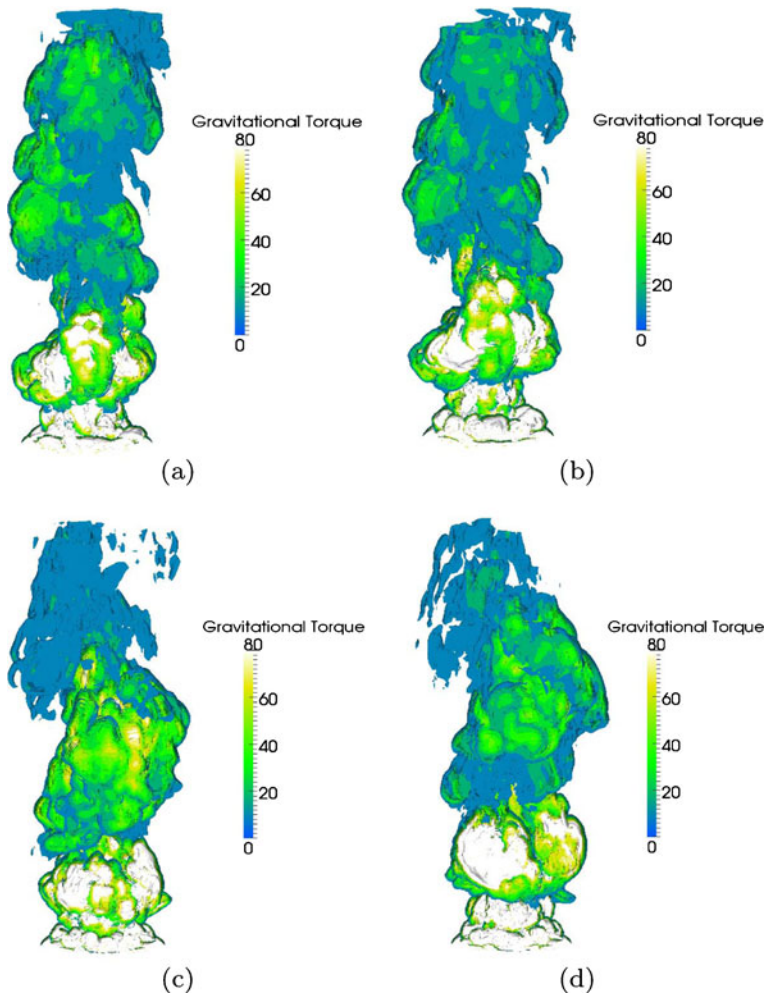


Fig. 5 Instantaneous snapshots of puff cycle showing isosurfaces of gravitational torque magnitude at 1 % of the maximum value at times **a** 10.2 s, **b** 10.26 s, **c** 10.74 s and **d** 11.02 s.

torque is observed at the base of the plume, reaching values up to $\approx 8000 \text{ s}^{-2}$. Of similar importance is the influence of baroclinic torque, presented in Fig. 6. The maximum baroclinic torque is located in regions where large pressure and density gradients are present, reaching values up to $\approx 5000 \text{ s}^{-2}$ at the base of the plume. Both these torques initiate the base instability and then promote its rapid growth. For large plumes and pool fires, this vortex quickly destabilizes, forming secondary azimuthal, or ‘finger-like’, instabilities similar to the ones reported in smaller scale experimental studies [26]. The formation of secondary instabilities creates streamwise vorticity that serves to promote the breakdown of large-scale toroidal structures and enhances local mixing processes.

The influence of each of the five terms in the vorticity equation (Eq. 11) is shown in Fig. 7 for the fine grid with SGS model. It is clear that, at height $y = 0.0 \text{ m}$,

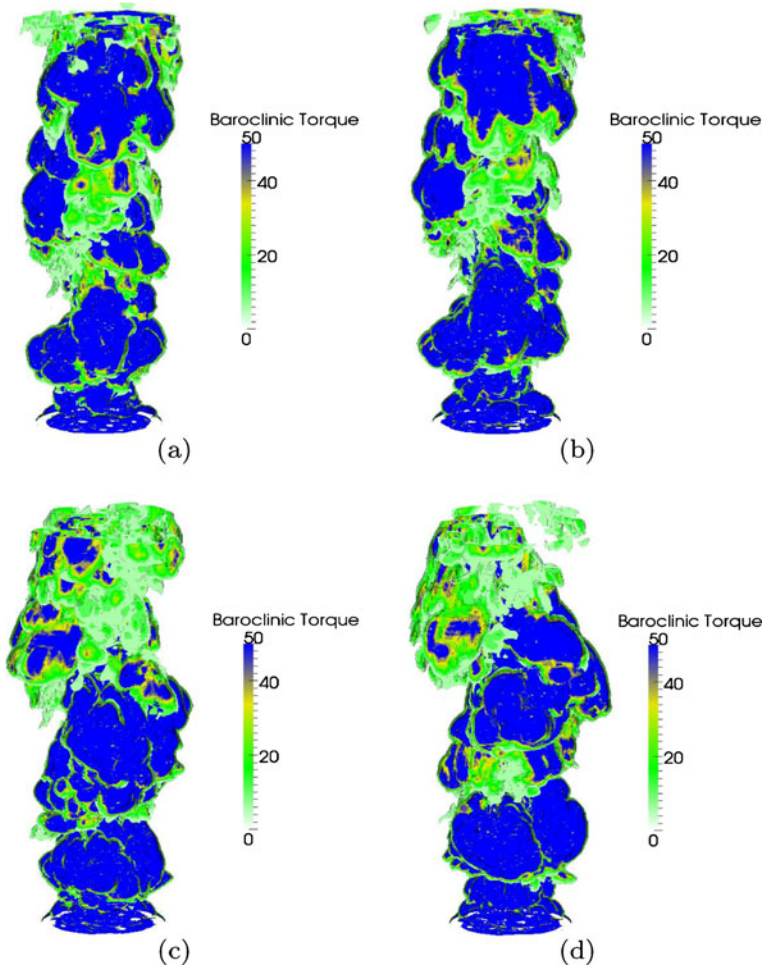


Fig. 6 Instantaneous snapshots of puffing cycle showing isosurfaces of baroclinic torque magnitude at 1 % of the maximum value at times **a** 10.2 s, **b** 10.26 s, **c** 10.74 s and **d** 11.02 s

the generation of instabilities is maximum at the edge of the plume ($x = \pm 0.5$ m), creating a net maximum vorticity of 1300s^{-2} . At this location, vorticity is also generated about 0.1 m away from the centerline, where a net vorticity of 1200s^{-2} is observed. This is where the Rayleigh-Taylor instability is triggered, causing a mass of helium to be convected downstream (Fig. 3). Higher in the domain the influence of the gravitational torque and vortex stretching decreases while the influence of the baroclinic torque and the dilatation term increases, causing the vorticity field to expand and reduce its magnitude.

5.3 Puffing frequency

The effect of grid spacing and SGS modelling on the puffing cycle of the helium plume is presented in Fig. 8, showing time traces of the centerline streamwise velocity

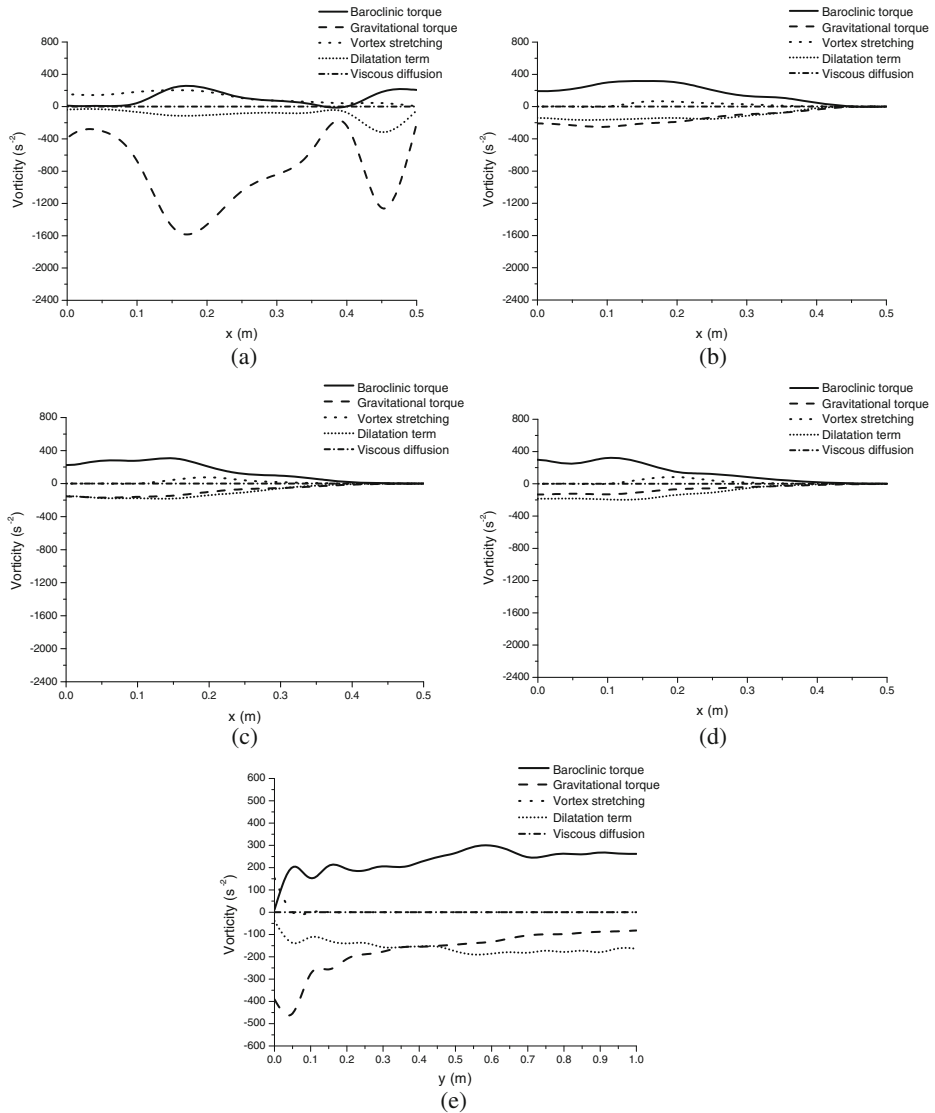


Fig. 7 Vorticity budgets from Eq. 11 for the fine grid with the Smagorinsky SGS model at **a** $y = 0.0$ m, **b** $y = 0.2$ m, **c** $y = 0.4$ m, **d** $y = 0.6$ m and **e** on the centerline up to $y = 1.0$ m

at location $y = 0.5$ m above the inlet, for a total of 5 s in the simulations. The puffing frequency corresponds to the number of puffing cycles encountered, a maximum peak in the streamwise velocity followed by a minimum, in the given timeline examined. The simulation results revealed a phase shift in the periodic cycles, as compared to the experiments. Therefore, the time signals in Fig. 8b have been shifted along the time axis to make the comparison with the experiments more clear. For the coarse mesh, low frequency large scale puffing can be observed with the use of SGS model. Without SGS model a higher frequency mode is more obvious and the

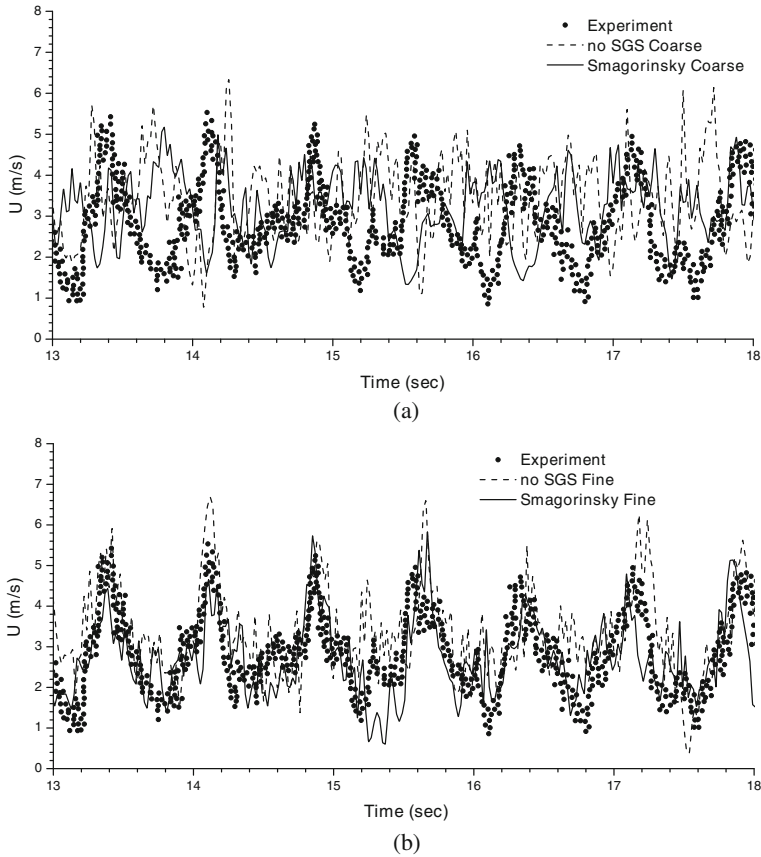


Fig. 8 Time trace of centerline streamwise velocity at $y = 0.5$ m above the base of the plume for **a** coarse grid and **b** fine grid

puffing frequency is hard to identify. As the mesh is refined, a clear puffing frequency is evident. Regardless of the use of a SGS model, a total of 7 cycles, corresponding to the passage of large turbulent structures, are distinguished, followed by an occasional smaller puff. The use of the SGS model reduces the dynamic range (defined as the difference between the maximum and the minimum results observed) of the streamwise velocity due to the damping of the flow, as has also been reported in [13]. More fluctuations appear when no SGS model is applied.

The puffing frequency results, are further analyzed, using the software package Grace (<http://plasma-gate.weizmann.ac.il/Grace/>) to produce a Fourier transformation on the time signal, taken over the last 10 s in the simulation, of the streamwise velocity on the centerline at $y = 0.5$ m. The result is presented in Fig. 9. For the coarse grid without SGS model, there is no clear peak. The highest peak in the puffing frequency prediction is at 2.31 Hz, but there is e.g. also a peak at 1.29 Hz. When the SGS is applied, the frequency peak is clear at 1.11 Hz. The influence of the SGS is clear, but the agreement with the experimentally observed frequency is not satisfactory. The experimental puffing frequency obtained by O'Hern et al. [14]

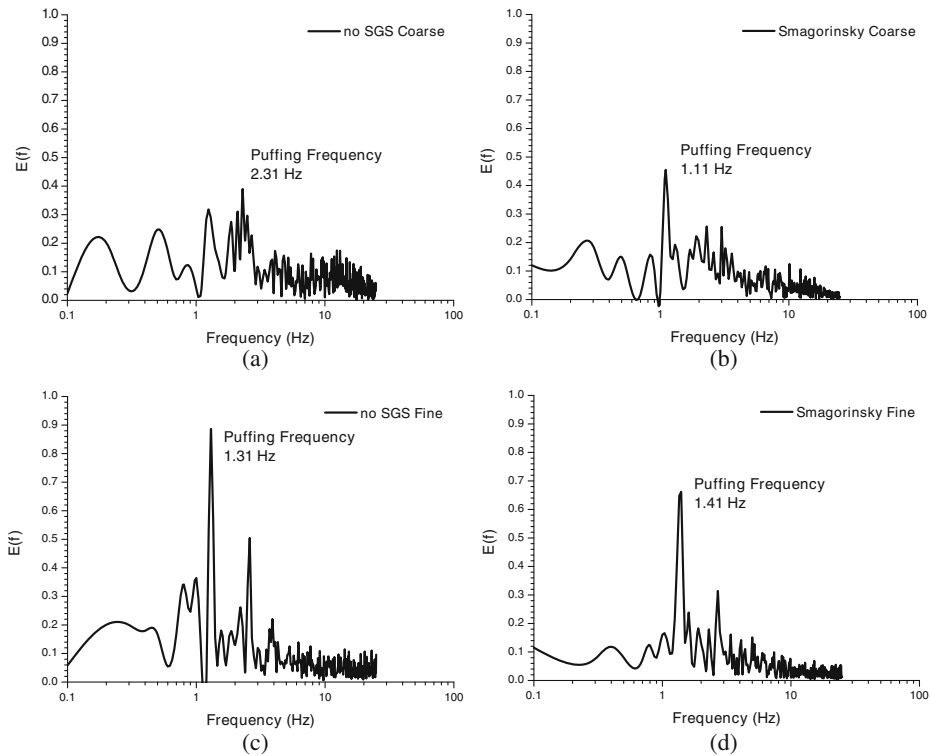


Fig. 9 Power spectrum of streamwise velocity on the centerline at $y = 0.5$ m above the base of the plume for coarse grid with **a** no SGS, **b** Smagorinsky model and fine grid with **c** no SGS, **d** Smagorinsky model

is 1.37 ± 0.1 Hz. The experimental correlation, $f = 0.8 Ri^{0.38} U_P / D_P$, suggested by Cetegen et al. [6] for $Ri < 100$, leads to a puffing frequency of 1.34 Hz for the set-up at hand, while the established puffing frequency correlation for buoyant diffusion flames of various fuels by Cetegen et al. [5], $f = 1.5 / \sqrt{D_P}$, yields a frequency of 1.5 Hz, independent of flow conditions. On the fine grid, a distinct peak around 1.31 Hz for the case without SGS model is found. This peak shifts to 1.41 Hz when the SGS model is applied. The influence of the SGS model is not very large on the fine mesh (see also Section 6) and the results agree very well with the correlations mentioned.

5.4 Mean and rms values for velocities and helium mass fractions

Results for the mean values and higher order statistics are presented in this section. The shaded area in the graphs represents the experimental uncertainty, as described in Section 3.

Figure 10 presents the centerline profiles of mean and rms of the streamwise velocity components up to $y = 0.8$ m above the base of the plume. For the mean values, all simulation results remain within the experimental uncertainty at practically all locations. Best agreement is observed on the fine mesh with SGS model. For the rms values also good agreement is observed, especially when the SGS model is applied.

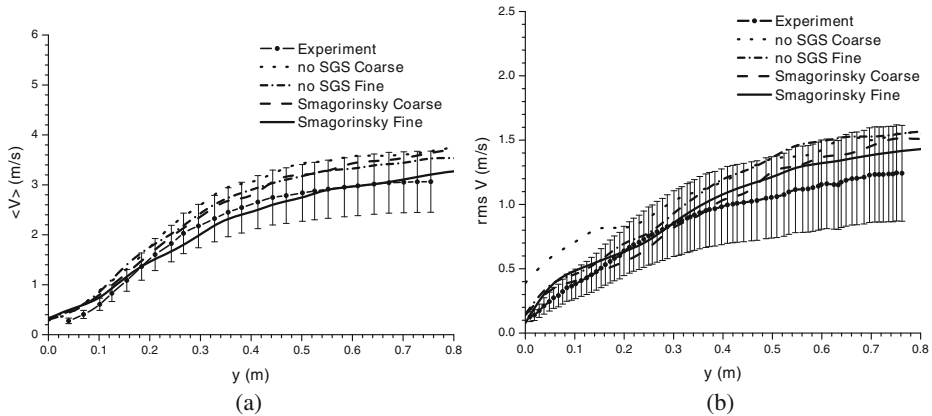


Fig. 10 Comparison of density-weighted, time-averaged **a** mean and **b** rms values for the centerline streamwise velocity up to $y = 0.8$ m above the base of the plume

Overall all simulation results remain within experimental uncertainty (except for the coarse grid case without SGS model, where the rms values are over-predicted close to the inlet).

The mean and rms values for helium mass fractions on the centerline up to a height of $y = 0.8$ m are presented in Fig. 11. Agreement is less satisfactory than for the flow field: the decay of the mean values is too slow in the simulations from $y = 0.2$ m onward. The rms values are over-predicted as well.

Results for the density-weighted, time-averaged streamwise velocities at several heights ($y = 0.2$ m, 0.4 m and 0.6 m above the inlet) are presented in Fig. 12. Generally at all three locations, the streamwise velocity is well predicted. Also noticeable is that downstream, away from the plume inlet, there is an increase in the streamwise velocity due to acceleration caused by buoyancy forces.

Figure 13 presents results for the density-weighted, time-averaged rms values of the streamwise velocities. The differences between the simulation results are small at

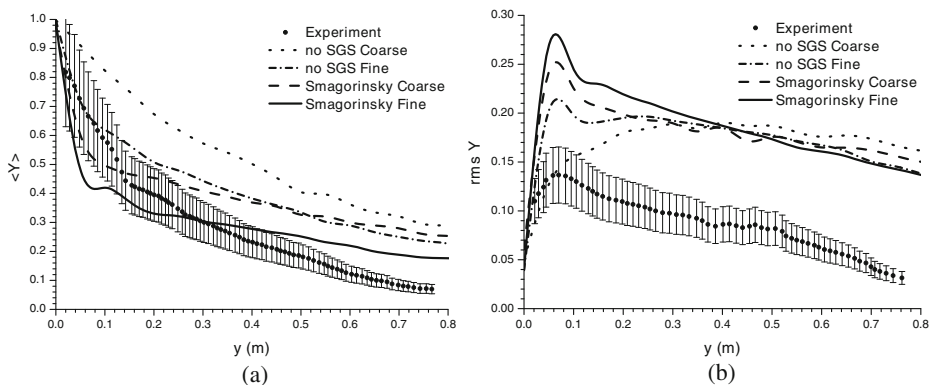


Fig. 11 Comparison of density-weighted, time-averaged **a** mean and **b** rms centerline values for the helium mass fraction up to $y = 0.8$ m above the base of the plume

Fig. 12 Comparison of density-weighted, time-averaged streamwise velocities at heights $y = \mathbf{a}$ 0.2 m, \mathbf{b} 0.4 m and \mathbf{c} 0.6 m

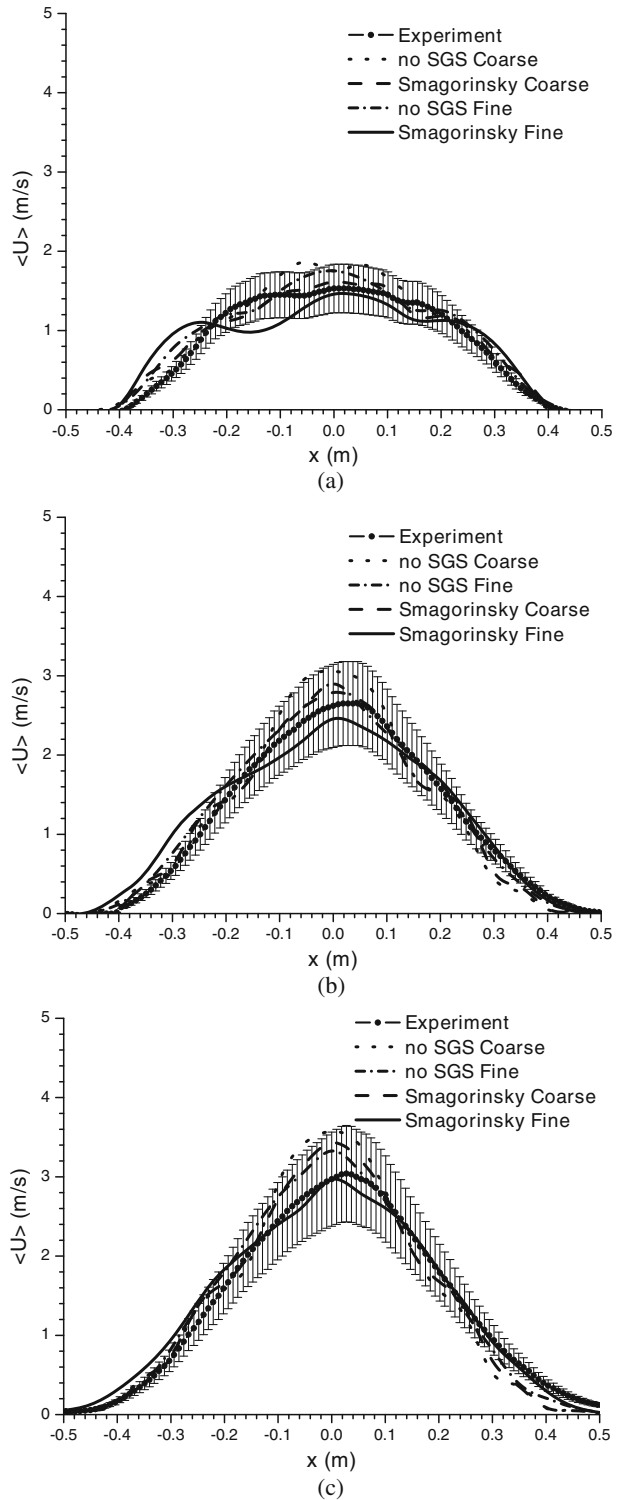


Fig. 13 Comparison of density-weighted, time-averaged rms streamwise velocities at heights $y = \mathbf{a}$ 0.2 m, \mathbf{b} 0.4 m and \mathbf{c} 0.6 m

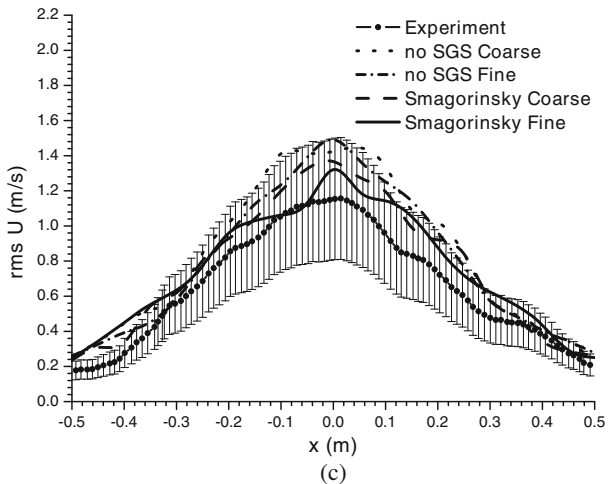
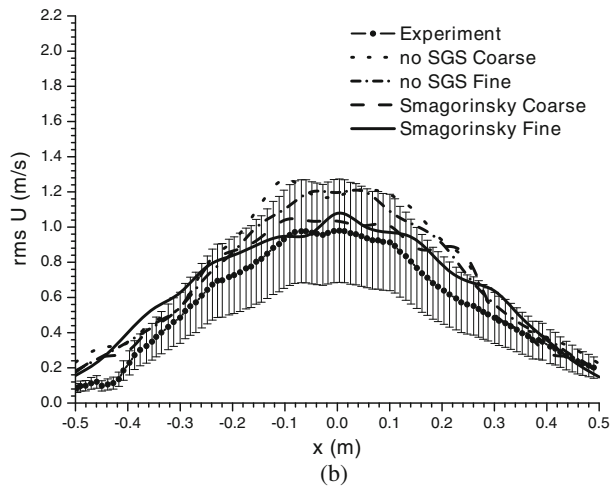
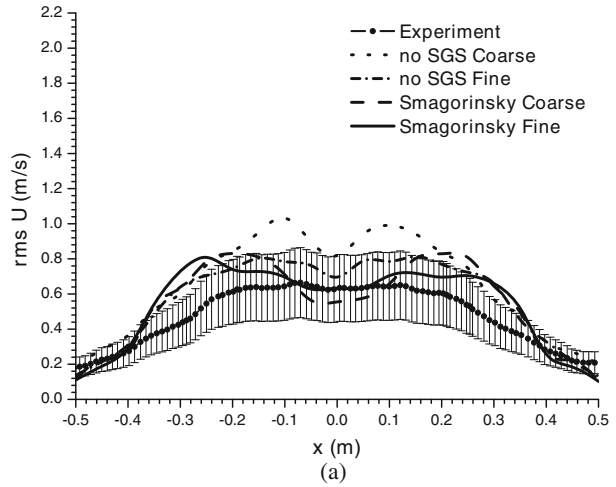


Fig. 14 Comparison of density-weighted, time-averaged cross-stream velocities at heights $y = \mathbf{a}$ 0.2 m, \mathbf{b} 0.4 m and \mathbf{c} 0.6 m

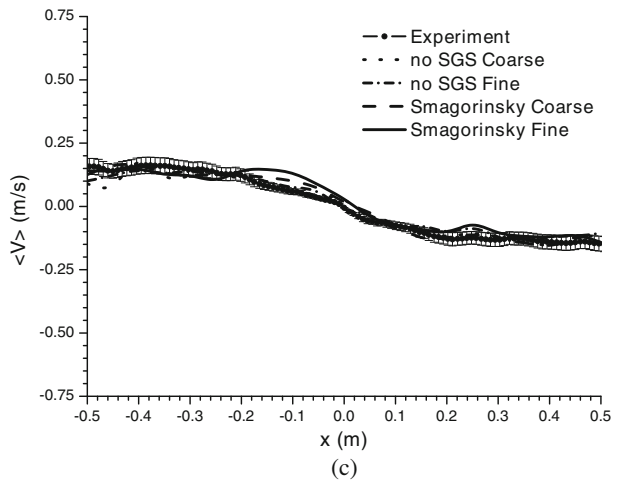
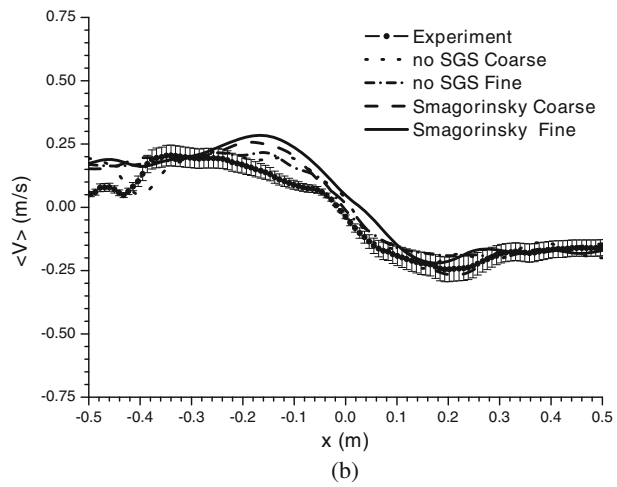
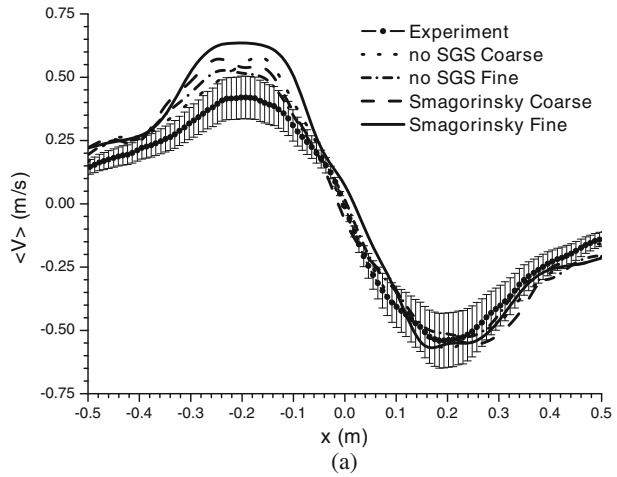


Fig. 15 Comparison of density-weighted, time-averaged rms cross-stream velocities at heights $y = \mathbf{a}$ 0.2 m, \mathbf{b} 0.4 m and \mathbf{c} 0.6 m

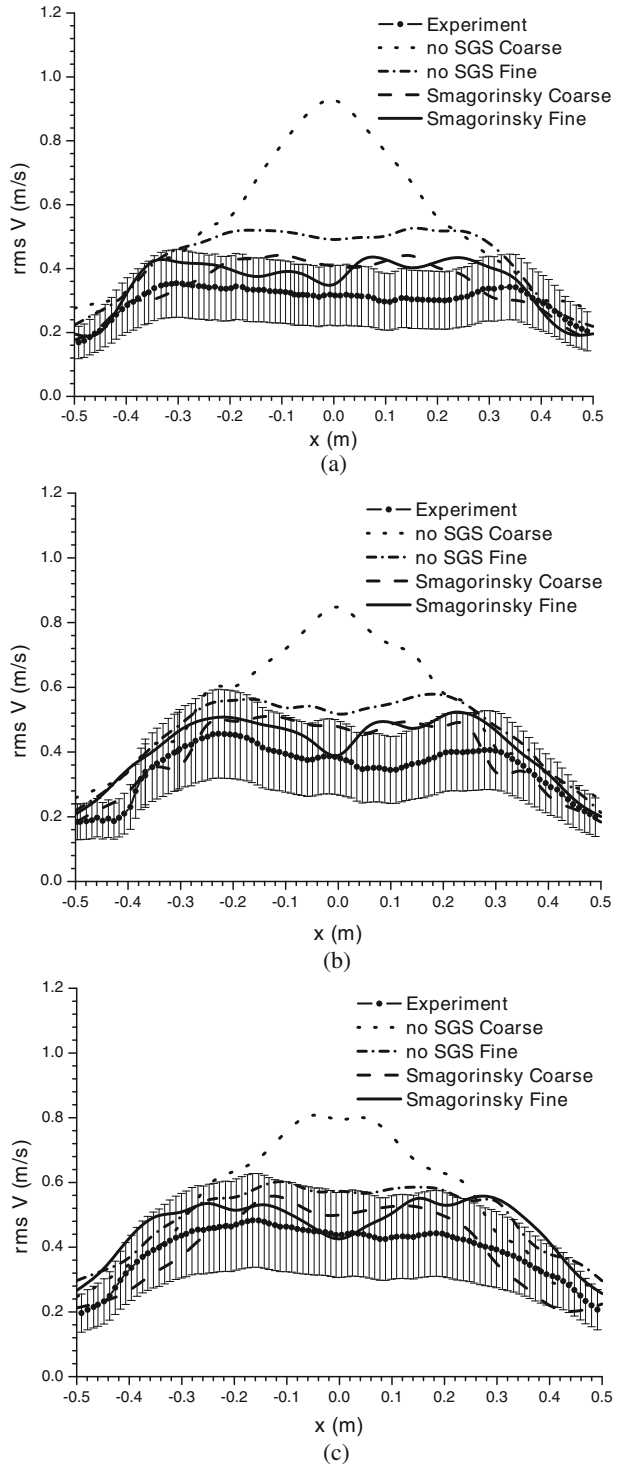


Fig. 16 Comparison of density-weighted, time-averaged mass fractions at heights $y = \mathbf{a}$ 0.2 m, \mathbf{b} 0.4 m and \mathbf{c} 0.6 m

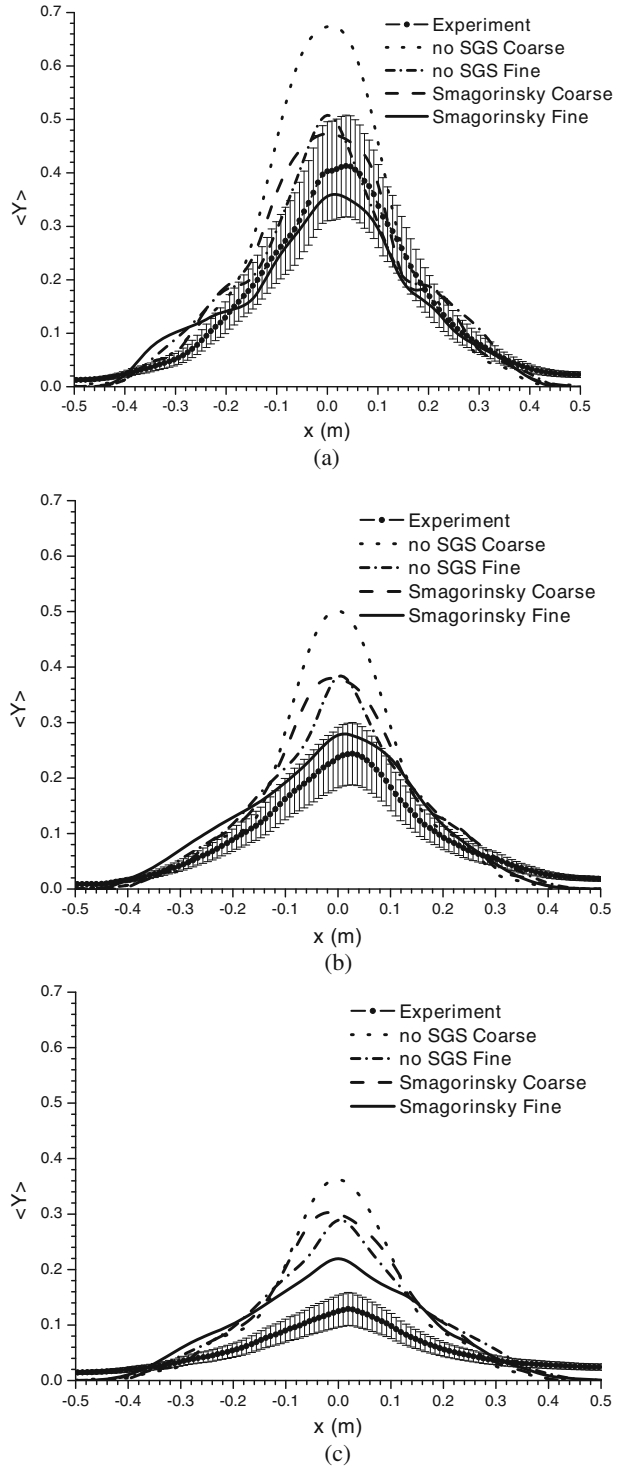


Fig. 17 Comparison of density-weighted, time-averaged rms mass fractions at heights $y = \mathbf{a}$ 0.2 m, \mathbf{b} 0.4 m and \mathbf{c} 0.6 m

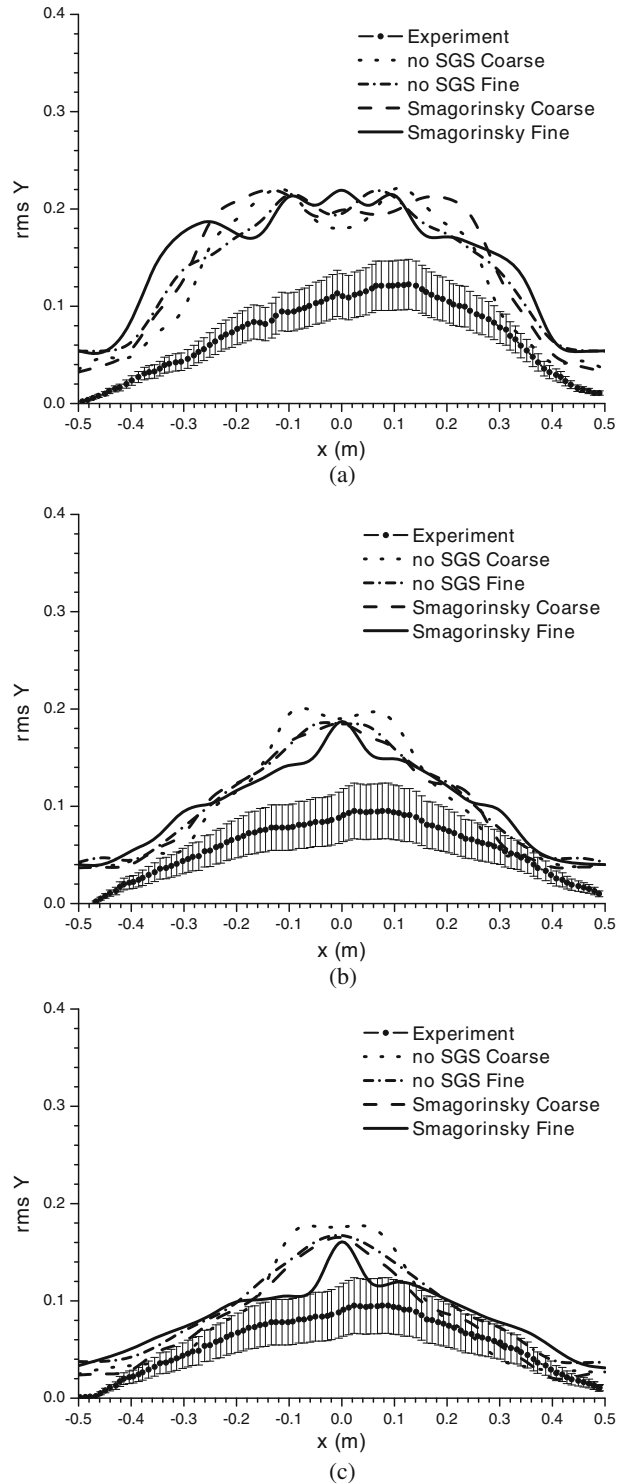


Fig. 18 Comparison of density-weighted, time-averaged product of rms streamwise and rms cross-stream velocities at heights $y = \mathbf{a}$ 0.2 m, \mathbf{b} 0.4 m and \mathbf{c} 0.6 m

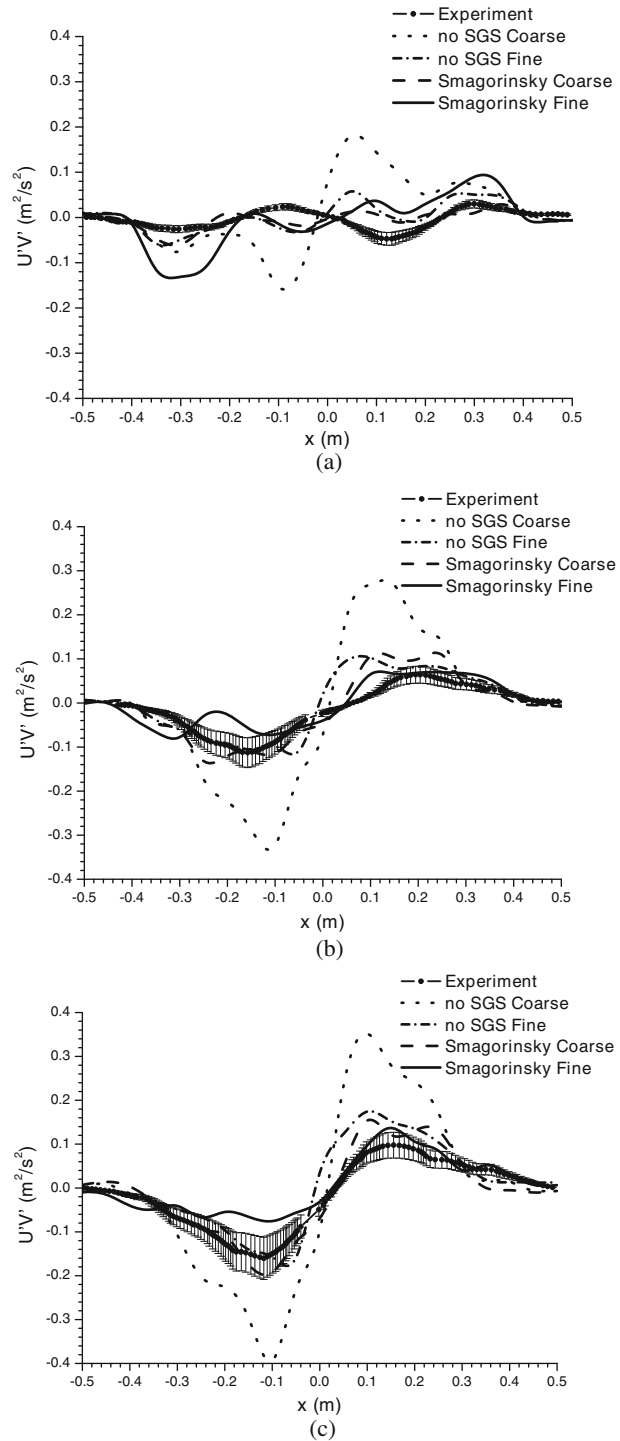
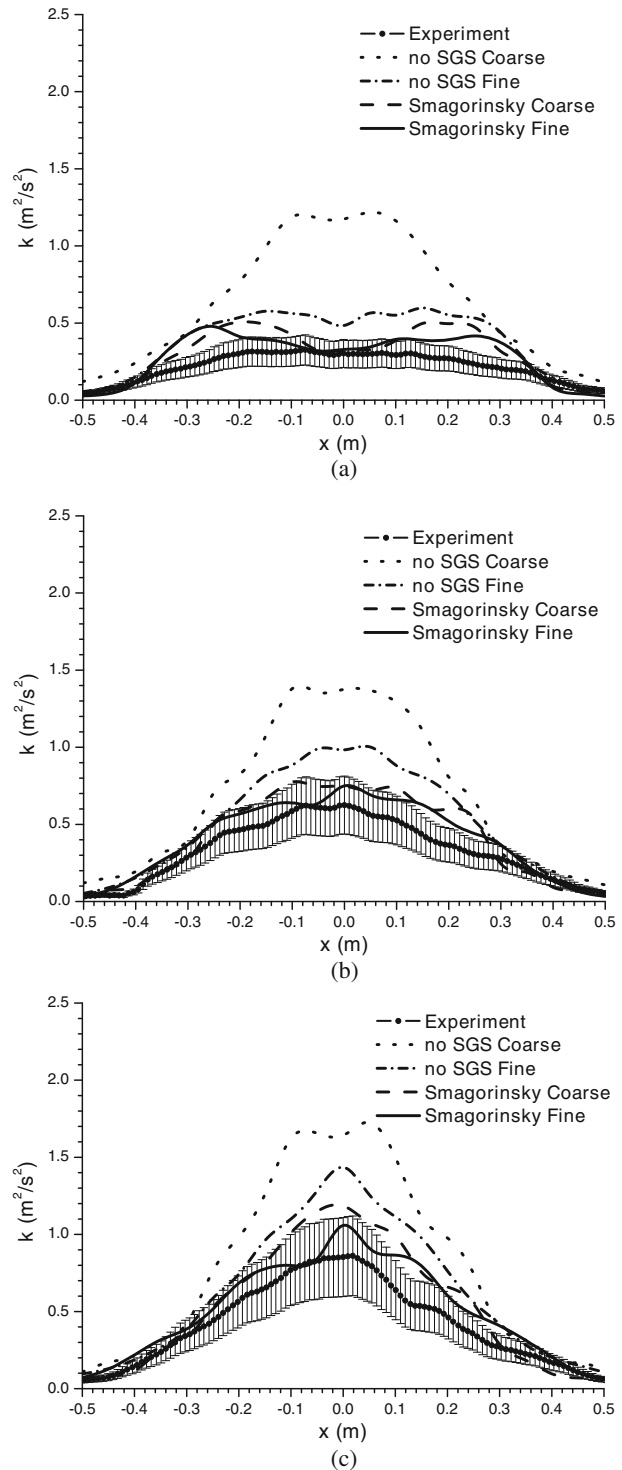


Fig. 19 Comparison of density-weighted, time-averaged turbulent kinetic energy at heights $y = \mathbf{a}$ 0.2 m, \mathbf{b} 0.4 m and \mathbf{c} 0.6 m



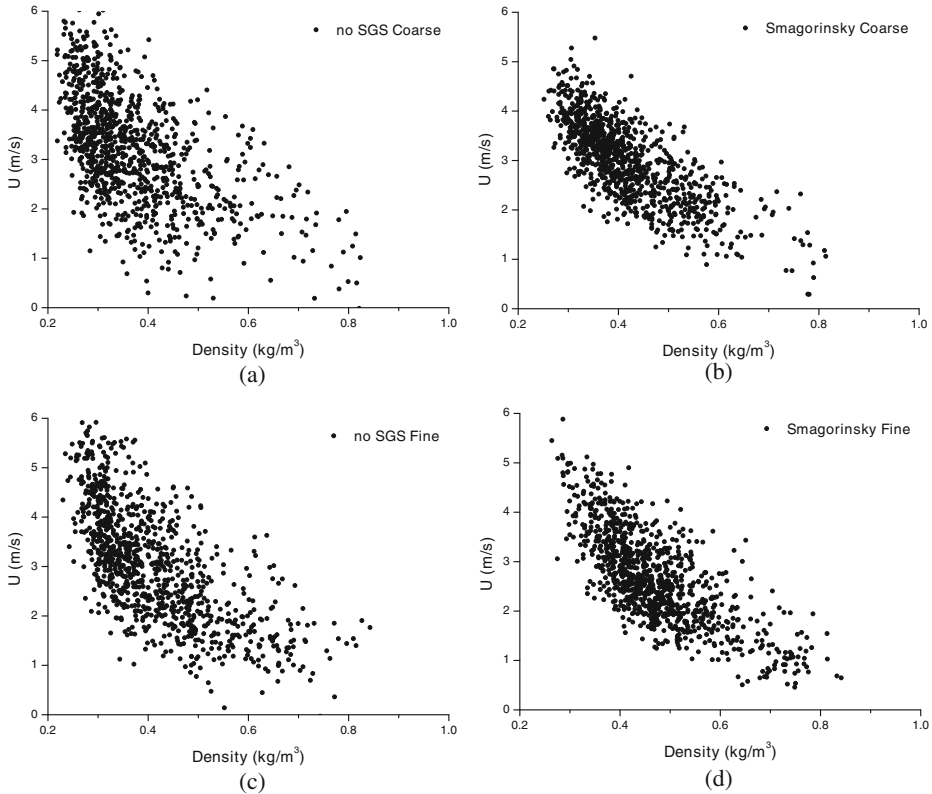


Fig. 20 Instantaneous vertical velocity component U vs density at $x = 0.03$ m, $y = 0.46$ m for coarse grid with **a** no SGS, **b** Smagorinsky model and fine grid with **c** no SGS, **d** Smagorinsky model

all heights. The cases with the fine grid show good agreement with the experiments, particularly when the SGS is applied.

For the cross-stream velocities, presented in Fig. 14, good agreement with the experiment is observed for all cases examined. A small over-prediction on the left hand side of the source, at locations around $x = -0.2$ m is observed. However, the experimental data are not perfectly symmetric. For obvious reasons, this asymmetry could not be predicted in the simulations. The application of a SGS model causes an increase in the cross-stream velocity at all three heights. Note that, as a consequence of mass conservation, an increase in the cross-stream velocities will result in an increase in the streamwise velocities. Accurate results for the cross-stream velocities are important because in this kind of flows entrainment controls mixing, a parameter very important in pool fires where combustion processes are mixing-controlled.

Figure 15 presents results for the density-weighted, time-averaged rms values of the cross-stream velocities at the same locations. Near the plume edge, the results do not differ much. In the central region, the results at the coarse mesh without SGS model are far off. Best agreement is observed with the use of SGS model, particularly at the fine mesh. It is evident from both Figs. 13 and 15 that the use of a fine mesh reduces the rms values in the central region, in better with the experiments.

The simulations with SGS model predict a bimodal shape for the rms cross-stream velocities, similar to what was observed by Chung et al. [11] and DesJardin et al. [13]. The use of a SGS model also reduces the rms values.

Figure 16 presents results of the density-weighted, time-averaged helium mass fractions. The mean mass fraction values are over-predicted on the centerline, with larger discrepancies higher in the domain. Best results are obtained, at all three locations, on the fine grid with the use of a SGS model. Without SGS model, diffusion is clearly under-estimated. The turbulent diffusion term, proportional to μ_{sgs}/Sc_t , is then indeed absent. Globally, the mass fraction values obtained with the current simulations agree more favorably with the experimental data as compared to previously published CFD studies [11, 13].

Figure 17 presents results of the density-weighted, time-averaged rms values of helium mass fraction. An over-prediction of the experimental values is observed close to the base of the plume, for all cases tested. These discrepancies reduce higher in the domain, with overall better agreement when the SGS model is applied.

Results of the density-weighted, time-averaged product of rms streamwise and rms cross-stream velocities, $U'V'$, are presented in Fig. 18. Except for the simulation on the coarse mesh with no SGS model, the results are very close to the experimental

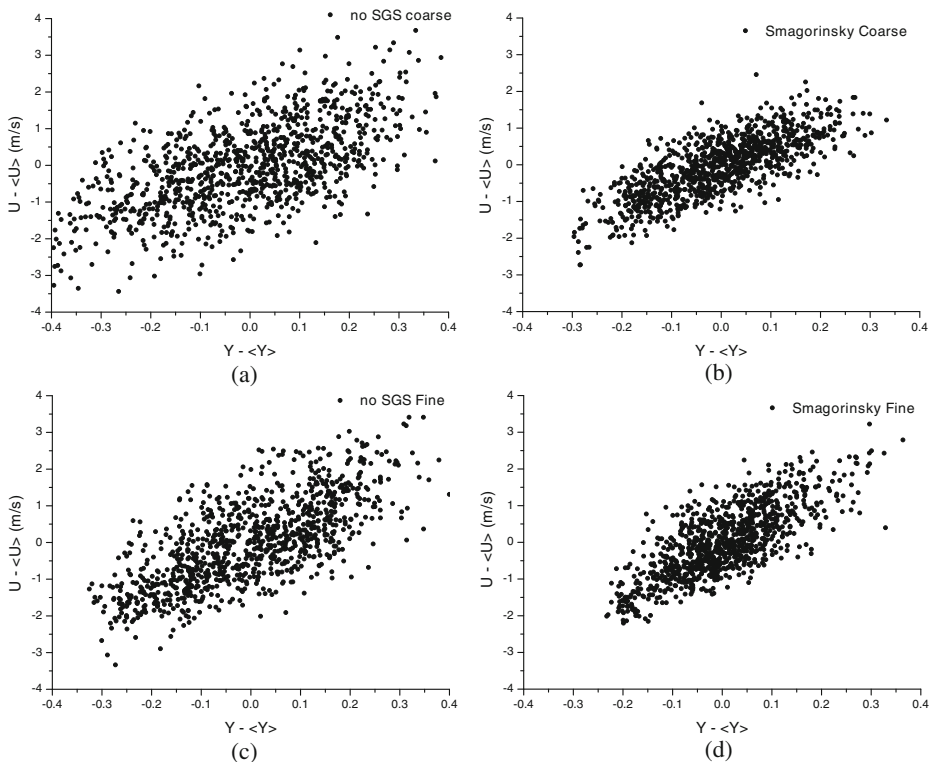


Fig. 21 $U - \langle U \rangle$ vs $Y - \langle Y \rangle$ at $x = 0.03$ m, $y = 0.46$ m for coarse grid with **a** no SGS, **b** Smagorinsky model and fine grid with **c** no SGS, **d** Smagorinsky model

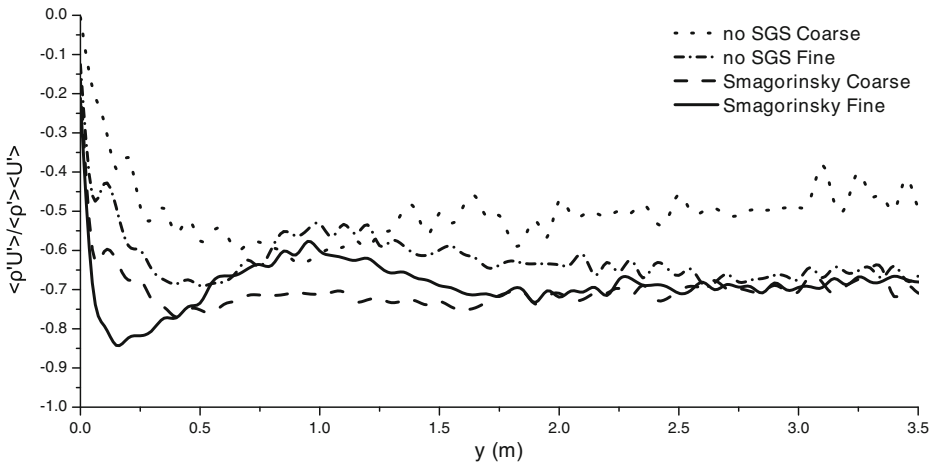


Fig. 22 Density - streamwise velocity correlation coefficient, $\overline{\rho'U'}/\sqrt{\overline{\rho'^2} \overline{U'^2}}$, up to $y = 3.5$ m above the base of the plume

values and the trends are captured, showing that the second order statistics in the present LES calculations are quite well predicted.

The density-weighted, time-averaged turbulent kinetic energy ($k = \frac{1}{2}[(\overline{U'})^2 + (\overline{V'})^2 + (\overline{W'})^2]$) results are presented in Fig. 19. At all three locations, the results on the fine grid with SGS model have the best agreement with the experiment. Without the SGS model the turbulent kinetic energies are over-predicted, especially near the centerline.

5.5 Correlation between velocity and density

Figure 20 shows scatter plots of instantaneous vertical velocity vs density at location $x = 0.03$ m, $y = 0.46$ m, as was reported in the experimental study of O'Hern

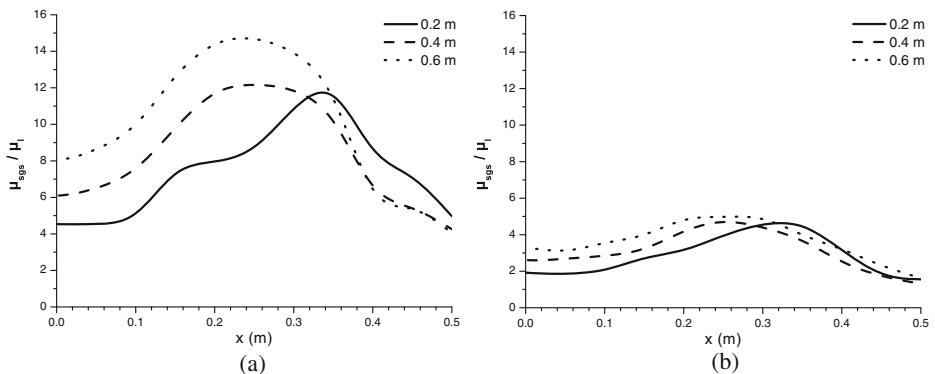
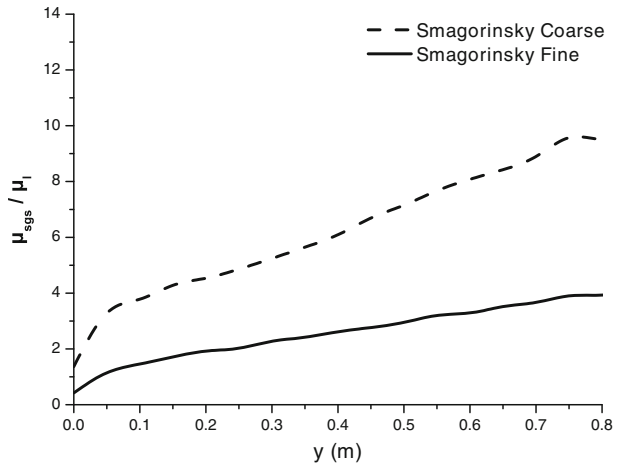


Fig. 23 Ratio of SGS to laminar viscosity, μ_{sgs}/μ_l , with the Smagorinsky model for the **a** coarse and **b** fine grid

Fig. 24 Ratio of SGS to laminar viscosity, μ_{sgs}/μ_l , with the Smagorinsky model on the centerline



et al. [14]. The strong anti-correlation between the streamwise velocity and density is confirmed. The maximum vertical velocities are observed in the low density region of the flow field. This is not surprising, as stronger acceleration can be expected in a lower density fluid for a certain differential pressure. When the SGS is applied, the scatter plot cloud is more dense and shifted towards higher density and lower streamwise velocity values, matching well the experimental measurements in [14].

Figure 21 shows essentially the same information by means of $(u - \tilde{u})$ and $(Y - \tilde{Y})$ correlation.

The spatial distribution of the density - streamwise velocity correlation coefficient, $\overline{\rho'U'}/\sqrt{\overline{\rho'^2}\overline{U'^2}}$, on the centerline up to $y = 3.5$ m above the base of the plume, is presented in Fig. 22. The correlation coefficient expresses the negative correlation

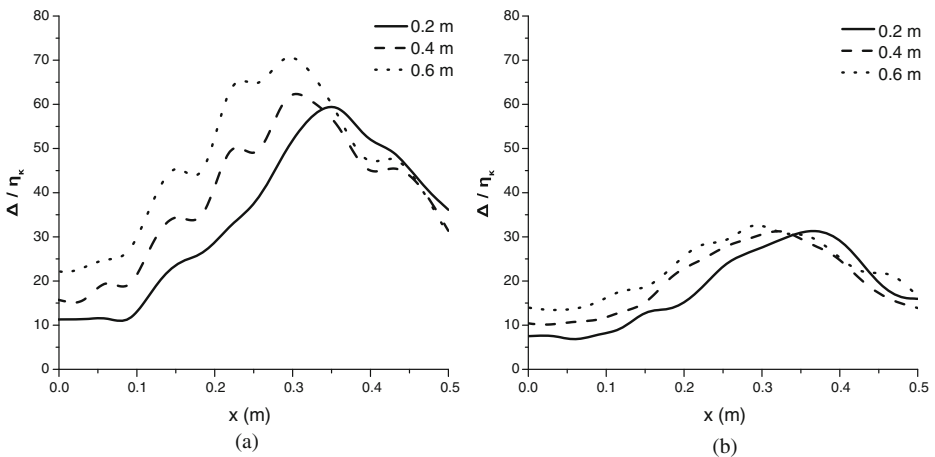


Fig. 25 Ratio of grid spacing, Δ , to Kolmogorov length scale, η_k , for **a** Smagorinsky coarse and **b** Smagorinsky fine

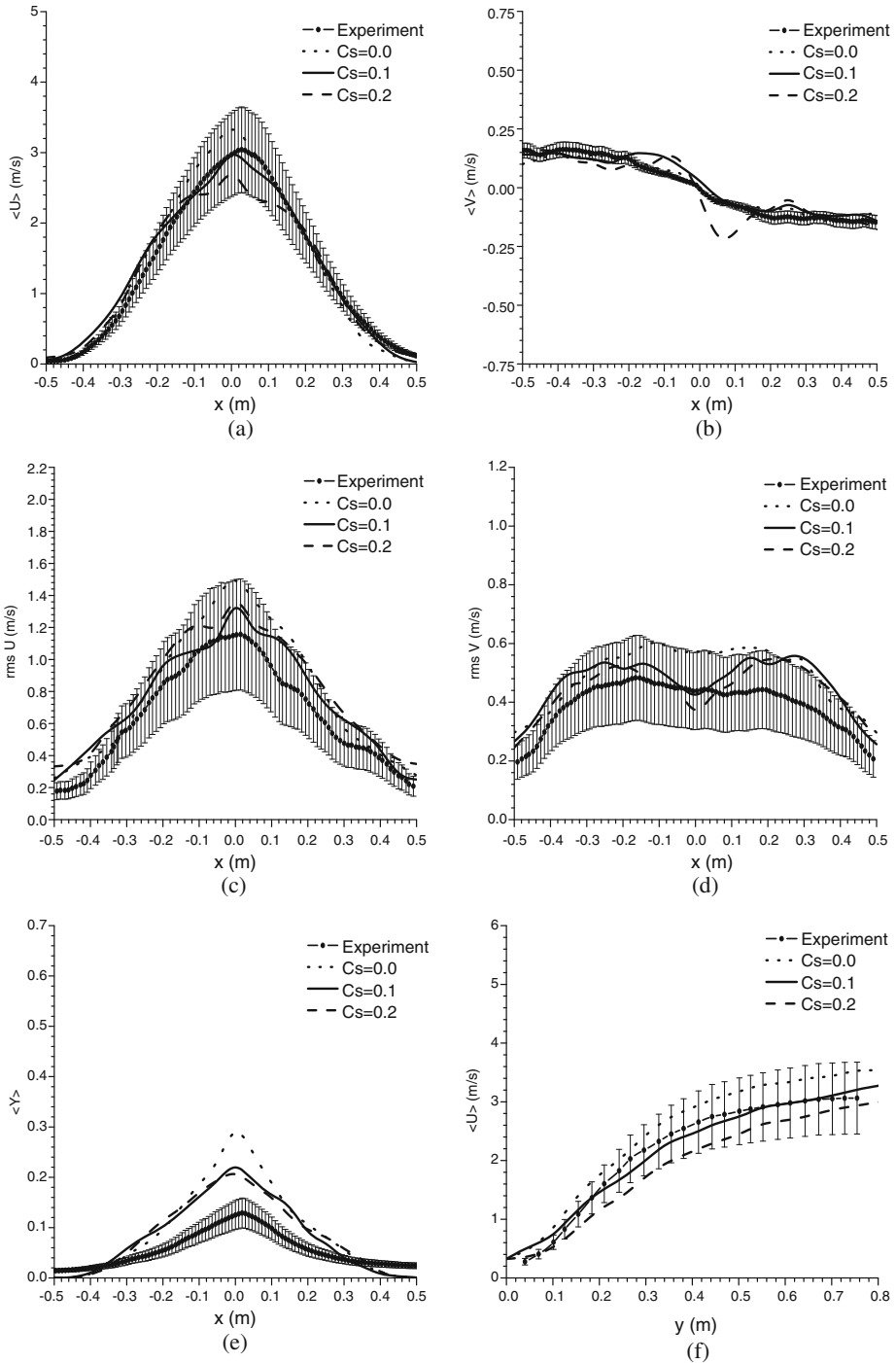


Fig. 26 Effect of Smagorinsky constant, C_s , in the fine mesh with turbulent Schmidt number, $Sc_t = 0.5$, at height $y = 0.6$ m on **a** streamwise velocity, **b** cross-stream velocity, **c** rms streamwise velocity, **d** rms cross-stream velocity, **e** mass fraction and **f** centerline streamwise velocity

between density and streamwise velocity. Sufficiently far away from the plume base, the value evolves to -0.7 (except for the results on the coarse mesh without SGS model). The value -0.7 agrees well with the small scale, thermal plume experiment by Shabbir and George [8].

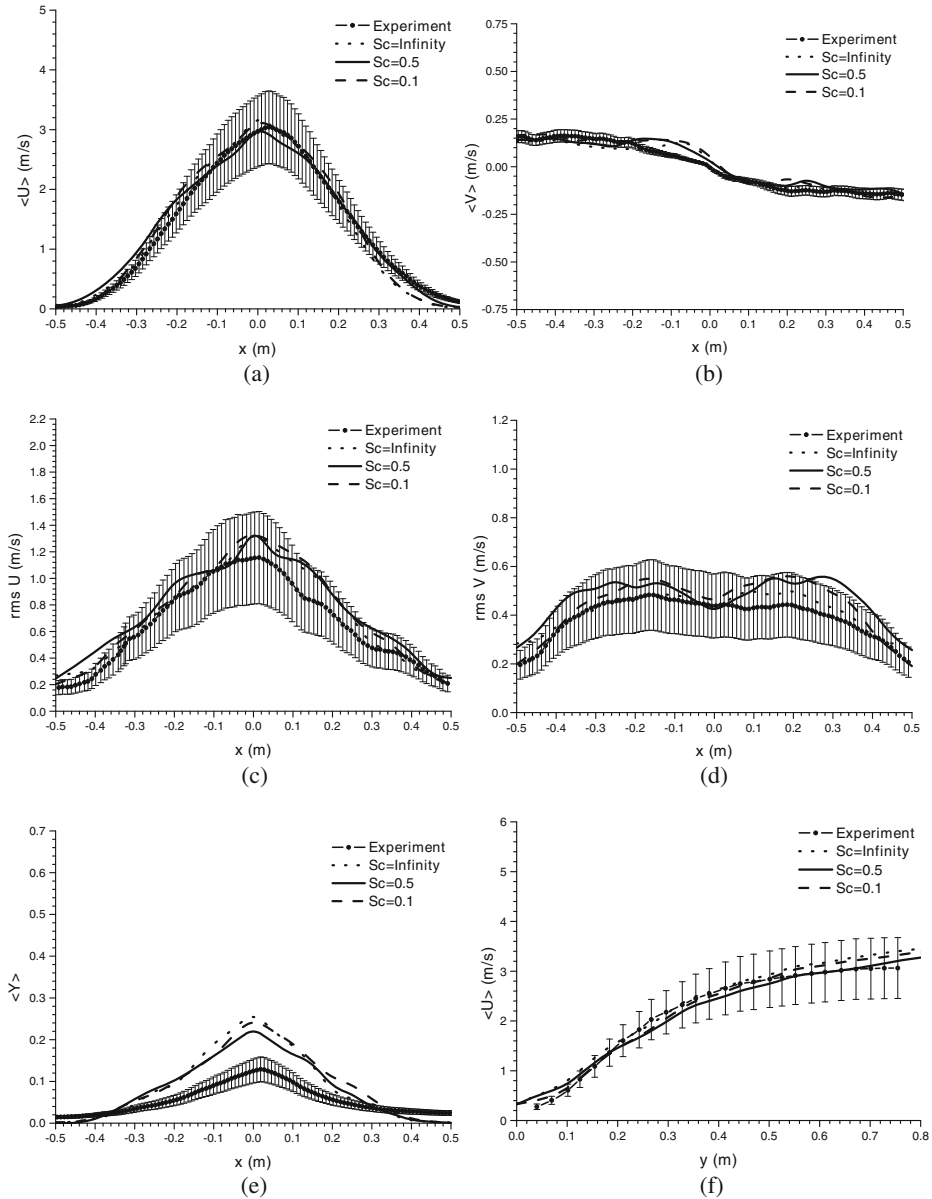


Fig. 27 Effect of turbulent Schmidt number, Sc_t , in the fine mesh with Smagorinsky model, $C_s = 0.1$, at height $y = 0.6$ m on **a** streamwise velocity, **b** cross-stream velocity, **c** rms streamwise velocity, **d** rms cross-stream velocity, **e** mass fraction and **f** centerline streamwise velocity

6 LES Resolution

The ratio of the SGS to laminar viscosity, μ_{sgs}/μ_l , is shown in Fig. 23. When compared to the coarse grid, the ratio on the fine grid is about 3 times smaller at the edge of the plume, where the generation of the instabilities occurs, and about 2–2.5 times smaller on the centerline. This is also seen in Fig. 24 showing that the ratio on the centerline increases with vertical distance from the plume base. This reveals that the influence of the SGS model on the fine grid is much smaller than on the coarse grid.

The ratio of grid spacing, Δ , to Kolmogorov length scale, $\eta_k = (\frac{\nu^3}{\epsilon})^{\frac{1}{4}}$, is presented in Fig. 25 for the near-field region of the plume, with the total dissipation rate expressed as $\epsilon = 2(\nu_l + \nu_{sgs})\bar{S}_{ij}\bar{S}_{ij}$. On the fine grid with the Smagorinsky model the ratio is about 10 to 15 on the centerline, depending on the vertical distance y examined, and goes up to 30 near the edge of the plume inlet, at $x = 0.35$ m.

7 Sensitivity Analysis

An important parameter in the LES calculations is the Smagorinsky constant, C_s , which controls the amount of dissipation introduced by the SGS model. The amount of dissipation is also related to the filter width, Δ , used in the simulations. As the grid becomes finer the amount of dissipation added by the SGS model decreases. Simulation results, for fine mesh, with Smagorinsky constants $C_s = 0.0, 0.1, 0.2$ at height $y = 0.6$ m are shown in Fig. 26. Best agreement is observed with Smagorinsky constant $C_s = 0.1$ for mean and rms results. Therefore, a Smagorinsky constant of $C_s = 0.1$ is a good estimate for this case. Results with $C_s = 0.0$ correspond to ‘no SGS’. Overall, the sensitivity on C_s is not substantial on the fine mesh, as could be expected from the previous section, where the high LES resolution was described.

The second parameter considered in this sensitivity analysis is the turbulent Schmidt number, Sc_t , used in Eq. 10 for the SGS species flux. In Fig. 27 results for various turbulent Schmidt numbers, $Sc = \infty$ (no SGS diffusion), $Sc = 0.5$ and $Sc = 0.1$ are presented, for the fine mesh with Smagorinsky constant, $C_s = 0.1$, at height $y = 0.6$ m. The variation of the turbulent Schmidt number does not have a strong influence on the simulation results.

8 Conclusions

In this study LES results for a large turbulent buoyant helium plume have been presented. The mechanism creating the characteristic puffing cycle of the plume has been analyzed and a qualitatively and quantitatively analysis of the instability generation, at the edge of the plume, mainly due to baroclinic and gravitational torque, has been presented.

The comparisons to experimental data reveal that for the near-field region of the plume, overall best agreement is obtained with the use of a SGS model. The puffing frequency, the mean and rms values of the velocity components obtained with FireFOAM are in very good agreement with the experiments. Agreement for the helium mass fraction (mean and rms) is less satisfactory, but in line with previously published results [11, 13].

The sensitivity analysis on the Smagorinsky constant, C_s , shows that $C_s = 0.1$ is a good choice. The fine mesh resolution has been shown to be such that the results do not depend strongly on the actual value of the Smagorinsky constant ($C_s = 0.1 - 0.2$). These observations contradict the conclusion in [13] that the use of a SGS model would not exhibit good predictions for the case at hand. The conclusions of the present study are in line with [11]. The impact of the turbulent Schmidt number, Sc_t , in the diffusion flux is very small.

Overall, the quality of the results is very satisfactory when compared to results previously published in the literature [11, 13] with other CFD packages, which is encouraging for the use of FireFOAM in future work for simulations of fire-induced flows.

Acknowledgements Very valuable were the discussions taken in the annual FM Global Open Source CFD Fire Modeling Workshop concerning FireFOAM and fire-related research topics.

References

1. Burton, G.C.: Large Eddy Simulation of a Turbulent Helium-air Plume Using the nLES Method. Center for Turbulence Research, Stanford University and NASA-Ames Research Center, Stanford, CA (2009)
2. Nicolette, V.F., Tieszen, S.R., Domino, S.P., Black, A.R., O'Hern, T.J.: A Turbulence model for buoyant flows based on vorticity generation. Technical Report SAND2005-6273, Sandia National Laboratory, Albuquerque, NM (2005)
3. Tieszen, S.R., Domino, S.P., Black, A.R.: Validation of a simple turbulence model suitable for closure of temporally-filtered Navier-Stokes equations using a helium plume. Technical Report SAND2005-3210, Sandia National Laboratory, Albuquerque, NM (2005)
4. Van Maele, K., Merci, B.: Application of two buoyancy-modified k- ϵ turbulence models to different types of buoyant plumes. *Fire Saf. J.* **41**, 122–138 (2006)
5. Cetegen, B.M., Ahmed, T.A.: Experiments on the periodic instability of buoyant plumes and pool fires. *Combust. Flame* **93**, 157–184 (1993)
6. Cetegen, B.M., Kasper, K.D.: Experiments on the oscillatory behaviour of buoyant plumes of helium and helium-air mixtures. *Phys. Fluids* **8**, 2974–2984 (1996)
7. Papanikolaou, P.N., List, E.J.: Investigations of round vertical turbulent buoyant jets. *J. Fluid Mech.* **195**, 341–391 (1988)
8. Shabbir, A., George, W.K.: Experiments on a round turbulent buoyant plume. *J. Fluid Mech.* **275**, 1–32 (1994)
9. Zhou, X., Luo, K.H., Williams, J.J.R.: Large eddy simulation of a turbulent forced plume. *Eur. J. Mech. B/Fluids* **20**, 233–254 (2001)
10. Soteriou, M.C., Dong, Y., Cetegen, B.M.: Lagrangian simulation of unsteady near-field dynamics of planar buoyant plumes. *Phys. Fluids* **14**, 3118–3140 (2002)
11. Chung, W., Devaud, C.B.: Buoyancy corrected k- ϵ models and large eddy simulation applied to a large axisymmetric helium plume. *Int. J. Numer. Methods Fluids* **58**, 57–89 (2008)
12. Pham, M.V., Plourde, F., Doan, K.S.: Direct and large eddy simulations of a pure thermal plume. *Phys. Fluids* **19**, 125103 (2007)
13. DesJardin, P.E., T.J. O'Hern, Tieszen, S.R.: Large eddy simulation and experimental measurements of the near-field of a large turbulent helium plume. *Phys. Fluids* **16**, 1866–1883 (2004)
14. O'Hern, T.J., Weckman, E.J., Gerhart, A.L., Tieszen, S.R., Schefer, R.W.: Experimental study of a turbulent buoyant helium plume. *J. Fluid Mech.* **544**, 143–171 (2005)
15. Weller, H.G., Tabor, G., Jasak, H., Fureby, C.: A tensorial approach to computational continuum mechanics using object orientated techniques. *Comput. Phys.* **12**, 620–631 (1998)
16. Wang, Y., Chatterjee, P., de Ris, J.L.: Large eddy simulation of fire plumes. *Proc. Combust. Inst.* **33**, 2473–2480 (2011)
17. Wang, Y., Chatterjee, P., de Ris, J.L.: Large eddy simulation of thermal and fire plumes. In: *Proc. of the Sixth International Seminar on Fire and Explosion Hazards*, pp. 267–278 (2011)

18. Smagorinsky, J.: General circulation experiments with the primitive equations. I. The basic experiment. *Mon. Weather Rev.* **91**, 99–164 (1963)
19. Poinso, T., Veynante, D.: *Theoretical and Numerical Combustion*. Edwards (2001)
20. Garnier, E., Sagaut, P., Adams, N.: *Large Eddy Simulation for Compressible Flows*. Springer (2009)
21. Blanchat, T.K.: Characterization of the air source and plume source at FLAME. Technical Report SAND01-2227, Sandia National Laboratory, Albuquerque, NM (2001)
22. Moin, P.: Advances in large eddy simulation methodology for complex flows, *Int. J. Heat Fluid Flow* **23**, 710–720 (2002)
23. Jiang, X., Luo, K.H.: Dynamics and structure of transitional buoyant jet diffusion flames with side-wall effects. *Combust. Flame* **133**, 29–45 (2003)
24. Jiang, X., Luo, K.H.: Spatial direct numerical simulation of the large vortical structures in forced plumes. *Flow Turbul. Combust.* **64**, 43–69 (2000)
25. Jiang X., Luo K.H.: Spatial DNS of flow transition of a rectangular buoyant reacting free-jet. *J. Turbul.* **2**, 1–18 (2001)
26. Weckman E.J., Sobiesiak, A.: The oscillatory behavior of medium scale pool fires. *Proc. Combust. Instit.* **22**, 1299–1310 (1988)